Title

THE DETECTION OP NEUTRON EXCESS ISOTOPES OP LOW Z ELEMENTS PRODUCED IN HIGH ENERGY NUCLEAR REACTIONS

Authors

Bowman, J.D.
Poskanzer, A.M.
Korteling, R.G.
et al.

Publication Date

1973-09-01

Submitted to
Phys. Rev. C.

LBL-1967
Preprint

THE DETECTION OF NEUTRON EXCESS ISOTOPES OF LOW Z ELEMENTS PRODUCED IN HIGH ENERGY NUCLEAR REACTIONS

J. D. Bowman, A. M. Poskanzer, R. G. Korteling, and G. W. Butler

September 1973

Prepared for the U. S. Atomic Energy Commission
under Contract W-7405-ENG-48

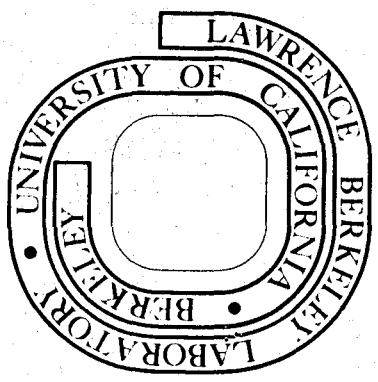

DISCLAIMER

THE DETECTION OF NEUTRON EXCESS ISOTOPES OF LOW Z ELEMENTS PRODUCED IN HIGH ENERGY NUCLEAR REACTIONS*

J. D. Bowman†, A. M. Poskanzer, R. G. Korteling‡, and G. W. Butler‡

Lawrence Berkeley Laboratory
University of California
Berkeley, California 94720

September 1973

ABSTRACT

A search was made for new isotopes of the elements lithium through nitrogen produced in the high energy (4.8 GeV) proton irradiation of a uranium target. The fragments were identified by ΔE-E and time-of-flight techniques. An electronic pulse width discriminator greatly reduced the background allowing high sensitivity. A new method for analyzing time-of-flight data and a new algorithm for particle identification were introduced.

Two new isotopes, ^{14}Be and ^{17}B, were observed to be particle stable, and the existence of ^{19}C was confirmed. It was shown that ^{12}Li and ^{16}B are particle unbound. Approximate production cross sections were determined for ^{14}Be, ^{17}B, ^{18}C, and ^{19}C, and upper limits estimated for ^{13}Li, ^{19}B, ^{20}C, and ^{22}N.

Keyword Abstract

NUCLEAR STRUCTURE ^{14}Be, ^{17}B, ^{19}C; particle bound.
^{12}Li, ^{16}B; particle unbound.

I. INTRODUCTION

The sudden interest in the field of neutron excess isotopes of low Z elements began in 1965 with the discovery[1] of ^{8}He in fission and the measurement of its half life[2] when produced in a high energy nuclear reaction. With the discovery[3,4] of ^{11}Li, ^{12}Be, ^{14}B, and ^{15}B the advantages of high energy nuclear reactions for the production of exotic nuclei became evident. These advantages include the high cross sections for the neutron excess isotopes and the nonspecificity of the reactions. Since then high energy nuclear reactions and counter telescope techniques have been used to discover ^{17}C,[5] ^{19}N, and ^{21}O,[6] and tentatively ^{19}C.[7] This method has also shown ^{10}Li [4] and ^{13}Be [5] to be particle unbound. High energy nuclear reactions combined with an on-line mass spectrometer have been used[8-11] to discover $^{27-33}$Na and $^{48-51}$K. Another fruitful method for the production of exotic nuclei has been heavy ion transfer reactions, which were used to discover[12-15] twenty-eight isotopes of the elements carbon through chlorine. These workers[16] also presented evidence for the particle instability of ^{14}Be, but this is contradicted by the present work[17] using high energy nuclear reactions. The present experiment presents the discovery of ^{14}Be and ^{17}B, confirms the existence of ^{19}C, and shows ^{12}Li and ^{16}B to be particle unbound.

The above described experiments are concerned with the particle stability of nuclei. It is generally agreed that determining masses of nuclei far from beta stability is of fundamental importance to nuclear physics with applications to many other fields. If the nuclei are at the limits of particle stability then their mere existence or non-existence, as determined in counter experiments such as this one, sets meaningful limits on their masses and tests the predictions of mass formulas. The method most often used for predicting

the particle stability of nuclei in this region has been the mass relations of Garvey and Kelson[18-19] which have been fairly successful. However, the discovery of ^{11}Li in 1966 was a significant exception because it had been clearly predicted to be unbound at that time. Progress was made so that a few years ago it was believed that all particle stable isotopes of the elements up through boron had been discovered.[20-22] The situation changed a year ago when Thibault and Klapisch[23] recalculated the masses and predicted ^{17}B to be bound by 0.6 MeV and ^{19}B to be bound by 0.2 MeV. The present experiment was stimulated by this recalculation which predicted ^{17}B to be the lightest undiscovered bound isotope. Thus, while the discovery of ^{17}B was not unexpected, our discovery of ^{14}Be was doubly surprising: first because it had been predicted to be unbound by 1.5 MeV, and second because it had been concluded from the above mentioned heavy ion transfer experiment[16] that in all probability it was unbound.

The present study was designed to search for neutron excess particle stable nuclei at the limits of stability by ΔE-E and time-of-flight techniques. The cross sections expected from systematics[24] for new nuclei were only about 10/ to 20 μb. The difficulty of the experiment can be understood by considering the total number of fragments entering the telescope. From previous work[24] on the high energy proton irradiation of uranium it is known that the production cross sections are 0.85 b for all fragments from lithium to sodium, 4.4 b for helium isotopes, and probably 10 b for evaporation-like hydrogen isotopes. Also several barns of fission and spallation products are produced. Thus, it is necessary to identify uniquely one in 10^6 of the fragments entering the telescope. This sets severe requirements on resolution, tailing, and background rejection, and necessitates the collection and careful processing of an enormous amount of data.

A previous experiment[25] demonstrated the feasibility of the ΔE-E-TOF technique but background problems limited its sensitivity. The pertinent differences in equipment for the present experiment are given in Section II. A new pile-up rejection system based on pulse width discrimination is described in Section IID and Appendix A. It was incorporated to decrease the background and thereby increase the sensitivity of the experiment. As part of the data analysis described in Section IIIB, corrections to the time-of-flight data were made for the dead layer and the variation in collection time with depth of fragment penetration in the E detector. A refinement to the algorithm for particle identification is described in Section IIIC. The results, given in Section IV, reflect these improvements by extending the limits of known particle stability and by setting small upper limits on the production cross sections for nuclides now at the limits of detection.

II. APPARATUS

A. General

The 4.8-GeV external proton beam of the Bevatron bombarded a 28 mg/cm^2 uranium metal target inside a 36-inch diameter evacuated scattering chamber. The average beam intensity was 6×10^{11} protons/pulse, with a one-second long beam pulse occurring every six seconds. Fragments were identified in a ΔE-E telescope in which the two detectors were separated by 25 cm. The time of flight between the two detectors and the E signal were used to identify the mass number of the fragment, and the ΔE-E information was used to distinguish the elements. Many of the details of the experimental equipment have been previously published[24,25] and only significant differences will be explained here. The general technique of ΔE-E-TOF identification has also been used recently by other workers[26,27].

B. Detectors

Since the resolution of the apparatus depends primarily on the characteristics of the ΔE and E detectors, special care was taken in their fabrication. The atomic number resolution depends critically on the thickness uniformity of the ΔE detector, and therefore, in order not to degrade the inherent resolution of the ΔE detector, silicon wafers which were to be made into detectors were preselected as described in Appendix B.

The mass resolution depends primarily on the time resolution of the ΔE and E detectors. At the beginning of the experiment measurements were made on the rise time of each detector--preamplifier--shaping amplifier combination for alpha particles and for electronic pulses injected onto the detector by a fast rise time (1 nsec) pulser. A ^{148}Gd 3.18 MeV alpha source was used for the ΔE detector measurements and a ^{212}Pb 8.78 MeV alpha source was used for the E detector measurements. The charge injected from the pulser was matched to the alphas in each case. The results obtained from these measurements are summarized in Table I.

The pulser rise time is somewhat slower than the alpha particle rise time because of the finite rise time of the pulser itself. For these measurements and throughout the experiment, we applied bias voltages substantially over that necessary to deplete the detectors completely in order to decrease the charge collection times. The values of the minimum field listed in Table I were calculated from the net bias voltage minus the voltage needed to deplete the detector, divided by the thickness. The detectors were cooled with thermoelectric coolers in order to reduce leakage current, electronic noise, and charge collection time. An energy calibration for each detector was obtained by using the above mentioned alpha sources in conjunction with a precision pulse generator.

During the experiment the detector telescope was placed at 90° to the beam. This did not cause much loss in yield because the angular distributions are only slightly forward peaked[24]. The plane of the target was at 45°. The ΔE detector was located 17 cm from the target in order to avoid the halo of the beam, and the flight path to the E detector was 25 cm. A larger area rejection detector was positioned just behind the E detector. The ΔE and E detectors had sensitive areas of 5 × 7 mm and were collimated to 4 × 6 mm by copper collimators 0.5 mm thick.

C. Electronics

A schematic diagram of the electronic apparatus is shown in Fig. 1. Much of the equipment was the same as that used in an earlier experiment[25], but there were several significant changes, the most important of which was the addition of a pulse-width-discriminator system to complement the existing 50 nsec pile-up rejector. This will be described in Section D. The details of the fast preamplifiers, amplifiers and cross-over discriminators have been described[25], except that now the fast amplifiers clipped the pulses to a width of 70 nsec. The cables between the preamplifiers and amplifiers were 40 m long. The cables transmitting the fast signals were 7/8 in. diameter Heliax coaxial cable. The time-to-amplitude converter was started by the E discriminator signal and stopped by the delayed signal from the ΔE discriminator. The time of flight of a fragment (TOF) was relative to time zero (T_o) which was determined approximately at the beginning of the experiment with the pulser. This was sufficient for the on-line monitoring of the data, but for the final data analysis, done off-line, T_o was determined precisely from the real particle data. During the experiment two pulsers were used. Each was split and one side was appropriately attenuated

and delayed so that one pulser simulated a high-energy zero-flight-time fragment and the other a ^{14}C which deposited 10 MeV in the E detector. The dual pulsers were controlled by a relay system that switched from one pulser to the other between each beam burst. The pulser events ($\approx$ 2/sec) were tagged as they were written on magnetic tape to allow off-line editing and stabilization of the data. The system was set up to measure flight times from 10 to 30 nsec--adequate for fragments from Li through N in the energy range 10 to 60 MeV over the 25 cm flight path.

The ΔE and E energy signals, the analogue particle identifier (PI) signal, the time-of-flight (TOF) signal, the ΔE and E pulse-width-discriminator (PWD) signals, together with a clock signal relative to the start of each beam burst, were all digitized, sent to a small on-line computer, and then stored on magnetic tape. The time of day was also stored with each buffer on tape. Three different kinds of on-line oscilloscope displays were generated by the computer. The first was a histogram display of the analogue particle identifier signal in which adjacent elements could be resolved. Six sets of digital windows could be set on the particle spectrum, and for each of these one could display either the TOF spectrum, the calculated T_o spectrum (described in Section IIIB), or the calculated mass spectrum. The third type of display was histograms of the ΔE and E PWD signals and the energy spectrum in the E detector. Digital windows were set on the ΔE, E, ΔEPWD, EPWD, and TOF signals, and only events which satisfied these five requirements were displayed.

The gains of the ΔE and E systems were matched via pulsers once every 12 hours during the $3\frac{1}{2}$ week data collection period. In addition, the fast timing characteristics were carefully monitored by not only observing the on-line mass resolution but also periodically determining the peak position and the FWHM of the T_o spectrum for both the pulser and for ^{11}B fragments.

D. Pulse Width Discriminator

The function of the pulse width discriminator (PWD) is to perform pile-up rejection on the signals from each of the detectors on a time scale which is a fraction of their rise time. Conventional pile-up rejectors operate on times longer than the width of the clipped amplifier output and have a time resolution which is several times larger than the detector-preamplifier rise time. A pulse width discriminator has a pulse pair resolution which is of the order of the square root of the rise time times the square root of the time resolution for single events. The PWD which we used measured the time difference from leading edge to cross-over of shaped detector pulses[28]. Overlapping pulses appear wider and were discarded in the later data analysis. However, the width above a fixed discriminator level of a single pulse increases with its amplitude, and therefore to utilize fully the pulse-pair resolution, one must first correct the PWD output for walk with amplitude. Details of the theory of its operation are discussed in Appendix A. An expression for its pulse-pair resolution is derived and numerical estimates are carried out. Also the related problem of walk with energy is discussed.

III. DATA ANALYSIS

The data consisted of 1.25×10^7 events written on 40 magnetic tapes. The five essential quantities recorded for each event were ΔE, E, ΔEPWD, EPWD, and TOF. Tagged pulser events from two pulsers were recorded simultaneously with the data for real particles. Using the pulser events all the data was edited for drifts and stabilized. The philosophy of data analysis was to use contour plots to examine two parameters at a time. Then, using appropriately constructed

algorithms, the data were transformed to form a new contour plot. The algorithms were adjusted so that the data formed ridges parallel to one axis, and then could be projected on to the other axis to form a histogram. Thus, the five dimensional parameter space was reduced to a two parameter, charge vs. mass number, contour graph. Finally the background was studied in order to determine which region of the original five parameter space to accept.

A. Editing and Stabilization

First the data were inspected for drifts. This was done by plotting the centroids of each of the two pulsers for each of the parameters vs. time. These plots exhibited occasional discontinuities as well as other spurious but unexplained behavior. About 2% of the data were rejected on this basis. Then events were regrouped by stabilization periods, each of which contained 140 events from each of the two pulsers and several thousand data events, corresponding to about ten minutes of data taking (which was short compared to the time constants of the remaining drifts). The next step was to use the pulser simulated events to eliminate these small drifts. The pulser amplitudes had been adjusted so that one of the pulser peaks fell at each end of the ΔE, E and TOF spectra. This allowed two point stabilization of these three quantities. Both pulser peaks occurred near the lower end of the PWD spectra of each detector and one of them was arbitrarily selected for stabilization. First the centroids of both pulser peaks in all 5 parameters were calculated. Then, in order to eliminate wild events, the centroids were recalculated using only those events which fell within $\pm 4\%$ of full scale of the raw centroids. New tapes were written for which the real data within each of the stabilization groups was shifted by linear transformations to fix the edited pulser peaks for each parameter at their nominal positions. This procedure reduced the effect of the small instabilities in the electronics, but was essential to combining the data collected over a long period of time.

The data analysis was now approached as three partially independent and parallel tasks: the determination of the mass number for each event, the determination of the nuclear charge for each event, and the editing of each event according to the ΔE and E PWD signals. The ΔE and E signals were expressed in MeV by a linear calibration, and the TOF signal was converted to T in nsec by a calibration curve with a small second order term measured with a precision delay box.

B. Determination of Mass Number

The determination of the mass number is based on the nonrelativistic equation[29], $E = \frac{1}{2} A m_o v^2$. Since the distance between the two detectors is known and the time of flight of each event is measured as well as its energy in the E detector, its mass number can be calculated as

$$A = \frac{2E}{m_o D^2} (T - T_o)^2 \qquad (1)$$

where T_o is an unknown zero of time. It was necessary to determine T_o directly from the real particle data. Our approach to this problem was to assume a value of the mass number A_o and to solve Eq. (1) for T_o. The events of a particular element were selected according to the PI signals as discussed in Section C, and the value of A_o was selected as that of the principal isotope of the element. This calculated estimate, T_z, of T_o is:

$$T_z = T - D \sqrt{\frac{A_o m_o}{2E}} \quad . \qquad (2)$$

The second term on the right side of Eq. (2) is the calculated time of flight, T_c, for a particle of mass number A_o and energy E. For events where the real

mass is equal to the assumed mass, a scatter plot of T_z vs. T_c should exhibit a grouping of the data forming a horizontal straight line at a value of T_z which gives T_o. If the real mass is not equal to the assumed mass, data points will cluster in families of straight lines which extrapolate to T_o as $T_c \to 0$, because $T_z - T_o = (1 - \sqrt{A/A_o})T_c$.

A contour plot representing such a scatter plot for boron isotopes is shown in Fig. 2(a). As suggested in the above arguments the different isotopes fall into distinct families. Although the family of curves are similar in shape they are by no means straight lines. We therefore investigated this problem and found that if three effects were taken into consideration the families became straight line extrapolations to the same intercept, and furthermore, the values of T_o determined for all isotopes of the elements Li through N were the same. The effects were: (1) the dead layer on the front of the E detector, (2) the different charge collection times for particles which penetrate the E detector to different depths, and (3) the walk of the ΔE discriminator with amplitude. These effects were included by modifying Eq. (2) to read

$$T'_z = T - D\sqrt{\frac{A_o m_o}{2(E + \delta E)}} + \phi\bar{R} + \varepsilon\Delta E \quad , \tag{3}$$

and the expression for the calculated time of flight becomes

$$T'_c = D\sqrt{\frac{A_o m_o}{2(E + \delta E)}} \quad . \tag{4}$$

Instead of using range-energy tables to calculate corrections (1) and (2), the ΔE and E data themselves, together with the power-law approximation to range-energy relations was used. The expression which results for the energy loss in the E detector dead layer is:

$$\delta E = \frac{\delta x}{x} \frac{(E + \Delta E)^b - E^b}{bE^{b-1}} \tag{5}$$

where δx is the E dead layer thickness, x is the ΔE detector thickness, and b is a dimensionless number. The expression for the average charge deposition depth in the E detector is:

$$\bar{R} = x \frac{b}{b+1} \frac{E^b}{(E + \Delta E)^b - E^b} \quad . \tag{6}$$

It was found that with suitable values of δx, ϕ, ε, and b, satisfactory T'_z vs. T'_c contour plots could be obtained as shown in Fig. 2(b). The ridge for ^{11}B is straight and horizontal and the other isotope ridges are straight and extrapolate to a common value of T_o. Furthermore, the fitted values of the parameters which are given in Table II are reasonable in terms of the physical effects which they account for. The mass number for each event was then calculated as follows:

$$A = \frac{2(E + \delta E)}{m_o D^2} (T + \phi \bar{R} + \varepsilon \Delta E - T_o)^2 \quad . \tag{7}$$

By taking a cut from Fig. 2(b) corresponding to energies between 18 and 22 MeV, the time resolution of our apparatus is obtained for ^{11}B particles which deposit 20 MeV in the E detector and 14 MeV in the ΔE detector. The histogram resulting from such a cut is shown in Fig. 3, which indicates that the FWHM time resolution is 290 psec. The pulser energy resolution in the E detector was only 120 keV and therefore the mass resolution found at mass 11 of 4.4% comes mainly from the time resolution.

The pulser time resolution was only 100 psec and may be compared with an estimate based on the characteristics of our preamplifiers. For the case which simulates the above mentioned ^{11}B fragment, the contribution of the E detector timing may be neglected because of its lower capacitance and the higher energy. Taking the capacitance of the ΔE detector as 160 pF, the 10-90% rise time as 2.5 nsec, the mutual transconductance (g_m) of the field effect transistor as 25 mA/V, and double delay-line shaping, one calculates a time resolution (FWHM) equal to 35 psec. On bench top tests 60 psec was achieved. The value of 100 psec at the accelerator during the experiment is not unreasonable. Also the pulse width discriminators had excellent time resolution for real particles as described in Section D. It was concluded that the 290 psec time-of-flight resolution for real particles was due to the gold contact layer on the detectors which had a sheet resistance of several ohms. It is thought that this resistance, together with the detector capacitance, caused an RC integration short compared to the rise time of the pulse, and the net effect was a variable delay depending upon the point at which the particle struck the face of the detector. It should be noted that an earlier experiment with a 17 μm ΔE detector had a resolution of only 170 psec.

C. Determination of Nuclear Charge

The Z determination proceeded in two steps. First the value of a particle identification (PI) algorithm was calculated from the ΔE and E signals of each event. Then the mass dependence of the calculated PI was removed using the mass number calculated in Section B. The PI algorithm is constructed so as to obtain a function of ΔE and E which depends only on particle type and not on ΔE or E separately. It should map families of curves in ΔE-E space into families

of straight lines parallel to the E axis in PI-E space. A contour plot of ΔE vs. E is given in Fig. 4. The algorithm, which is a modification of that used by Butler et al.[25], is:

$$PI = \sqrt{(\frac{E + \Delta E}{K})^p - (\frac{E}{K})^p} \tag{8a}$$

where

$$p = b - \frac{c}{x}\frac{\Delta E}{E} \quad . \tag{8b}$$

We found that the curvature in plots of PI vs. E could be removed over a wider range of elements and energies using a power, p, which decreased linearly with ΔE/E rather than just with ΔE as in Ref. 25. The values of the parameters used where b = 1.7, c = 0.1 mg/cm^2, and K = 300. Again, x is the ΔE detector thickness in mg/cm^2. A contour plot of our new PI algorithm vs. E is given in Fig. 5.

Figure 6(a) shows a histogram obtained by projection of Fig. 5 on the horizontal axis. The elements are separated from each other but the value of PI depends upon the mass as well as the nuclear charge. For example, an inspection of Fig. 5 shows that the Be group is divided into two peaks, one corresponding to ^{7}Be and the main peak to ^{9}Be and heavier isotopes, ^{8}Be being unstable. The heaviest isotopes of element Z are buried under the light isotopes of element Z + 1, which are produced in higher yield. This is the reason why an independent determination of the mass number by time-of-flight measurements is necessary. In order to determine the nuclear charge of each event it is necessary to remove this mass dependence of the PI signal, which is shown in Appendix C to be:

$$Z \propto PI/A^{0.3} \quad . \tag{9}$$

A histogram of Z is given in Fig. 6(b). The widths of the peaks have been reduced with ^{7}Be moved underneath the other isotopes of Be. The FWHM resolution in Z is 0.14 Z units. The peaks are not symmetric but exhibit a tailing towards low Z which will be of importance in the display of the results in Section F below.

D. Pulse Width Discrimination

The pulse-width-discriminator signals were used to edit out events affected by pile-up in either detector. The time walk with amplitude of the PWD signal over the range of energies which was accepted, was large compared to the intrinsic resolution of the instruments and was removed before the application of acceptance windows. It was found that the EPWD signal depended slightly on the type of particle and this dependence was also removed at this stage.

Figure 7(a) shows the walk with amplitude of the EPWD. It is shown in Appendix A that the amplitude dependence of the PWD signals is expected to be of the form

$$PWD \propto \mathcal{E}^{-1/q} \tag{10}$$

where $\mathcal{E}$ is the value of ΔE or E, and q is an integer. We determined the trend of the PWD signals by performing fits to scatter plots of PWD vs. $\mathcal{E}^{-1/q}$, and found q = 3. From plots of PWD vs. $\mathcal{E}^{-1/3}$, slopes and intercepts (α and β) were determined and used to define a normalized PWD signal (NPWD) as

$$NPWD = PWD - (\alpha + \beta\mathcal{E}^{-1/3}) \quad . \tag{11}$$

This form proved satisfactory for the ΔE signal but it was found that the E pulse width discriminator also had a shift with particle type which amounted

to 50 psec between Li and N. This shift results from the different charge collection times for particles which penetrate the E detector to different depths. It was removed by subtracting a term proportional to the average depth, $\bar{R}$, at which particles deposit their charge in the E detector as calculated in Section B. The normalized E pulse-width-discriminator signal was then calculated as

$$NEPWD = EPWD - (\alpha + \beta E^{-1/3}) - \gamma \bar{R} \qquad (12)$$

and a graph of NEPWD vs. E is shown in Fig. 7(b). Typical values of the parameters are given in Table III.

A histogram of yield vs. NEPWD is given in Fig. 8. After the determination of the parameters α and β for each tape, such a histogram was formed and the values of NPWD for which the yield was 1/4 of its maximum value were determined. If the central peak has a Gaussian shape with no background then 90% of the single events will fall in the acceptance region defined by these values. For the real data only 79% of the events fell within the windows of each PWD. Typical values for the FWHM and the FW$\frac{1}{4}$M are given in Table III.

E. Background Study

Before combining the 1.25×10^7 events into a two-parameter histogram of yield vs. nuclear charge and mass number, a study was carried out to determine what region of the 5-dimensional parameter space (ΔE, E, NΔEPWD, NEPWD, and T) to accept in order to obtain the best rejection of background events. A single data tape containing 4.5×10^5 events was processed to construct the contour plot of Z vs. A shown in Fig. 9(a) with all values of the parameters included. The density of background events in the high mass region on the

right side of Fig. 9(a) is appreciable and is comparable to the data of Butler et al.[25]. Figure 9(b) shows the factor of 80 improvement achieved by applying the PWD windows.

Scatter plots were made of NΔEPWD vs. ΔE and NEPWD vs. E for events falling into the high mass background rectangle indicated in Fig. 9(a). All events falling into this high mass background region are unphysical and result from random coincidences in one of the detectors. The E graph for these events is shown in Fig. 10. We have grouped the events into two categories indicated by A and B. Category A corresponds to coincidence events where two particles penetrate the ΔE detector and overlap in the E detector. When the E signal is small and comparable to the perturbing signal the EPWD signal is thrown far out. Category B, which extends up to 10 MeV, corresponds to events where a fragment and an alpha particle penetrate the ΔE detector but only the alpha particle hits the E detector. The yield of alpha particles is much larger than any other fragment and the maximum energy which they can deposit in the 67 μm E detector is 10 MeV. The contour plot of NΔEPWD vs. ΔE shows less structure. The points scatter about a horizontal straight line displaced about one standard deviation below the region corresponding to single events, and this small displacement is probably due to chance coincidences with alpha particles.

In view of the above considerations only events which deposited more than 10 MeV in the E detector were accepted, but the upper energy limit of 60 MeV, corresponding to the ESCA, was kept. Time-of-flight limits of $10.6 < T < 27$ nsec were imposed. From Fig. 4 it can be shown that this time-of-flight requirement is redundant with the E requirement for the heaviest isotopes of Be through N. These E and T windows selected out 60% of the events.

F. Final Data Displays

A rescaling of the mass and charge values was carried out for each tape before summing all data tapes. The experimental values of the masses of ^{9}Be and ^{13}C and the experimental values of the nuclear charges of isotopes of Be and C were determined for the first 10% of the events on each tape. A slight transformation of the charge and mass scales was then determined which caused these values to fall at predetermined values. This rescaling amounted to a small fraction of the intrinsic charge and mass resolution. At this time a tape containing 3% of the data was discarded because of poor resolution. Finally all data were summed into a two-parameter histogram of yield vs. nuclear charge and mass number: Fig. 11. Plotted in this figure are the 4.1 million events which survived all the selection criteria. Although this representation is complete, the isotopes will be more easily discernable when mass histograms are constructed for each element.

There are two kinds of tailing in Fig. 11. One is a tailing to low mass, evident for Be and B. This is due to a dead time in the E_{rej} circuitry which failed to eliminate all particles which passed through the active area of the E detector. Thus, some long range particles were recorded which deposited only part of their energy in the E detector. Since mass is calculated as Et^2, these events always tail to low mass and can be seen again in Figs. 14 and 15. The second kind of tailing, a tailing to low Z values, is a less obvious but more serious effect. It is noticeable in Fig. 11 but more clearly seen in Figs. 6(b) and 12, and is the cause of a small but discernable background trailing from one element ridge to the one lower. The origin of this tailing must come from a tailing in the ΔE signal because an error in the determination of E would

influence the mass as well as the charge. The possibility of slow charge collection was eliminated because of a lack of correlation of this effect with the ΔEPWD signal. Thin spots in the detector or channeling are other possible explanations. Since this low Z tailing was observed with several different detectors, the explanation based on channeling is most likely[30].

In order to construct mass histograms for each element from which relative yields could be estimated it was necessary to subtract this low Z tailing. Its shape was determined for those A values where a nuclide is known to be particle unstable. Figure 12 shows the charge distributions for mass cuts at masses 10, 13 and 16. The charge coordinate has been normalized to Be by scaling according to the FWHM of the peaks. In addition, the mass cut for A = 13 was normalized to A = 10 in intensity to compare directly the shapes for two different cases. Since both ^{10}Li and ^{13}Be are known to be particle unstable, these plots give directly the shape of the low Z tailing. The agreement between the two cases is sufficiently good that the average was used for the subtraction by normalizing at + $\frac{1}{2}$ Z. It amounted to a tailing at one Z lower of 0.3% for Be, 0.6% for B, 1.2% for C and 1.4% for N. Applying these corrections which were accurate to about 10%, mass histograms for Li through N were constructed and are illustrated in Figs. 13-17. For the C and N data the mass resolution was marginal and therefore tighter windows of only 12 to 34 MeV for E and 11.1 to 23.2 nsec for T, were used.

IV. RESULTS

The mass yield histograms, Figs. 13-17, show the existence of all previously known particle stable nuclei in this region except for ^{9}C. In addition,

two new nuclei, ^{14}Be and ^{17}B, are clearly observed and the stability of ^{19}C can be confirmed. Several criteria were considered to verify the existence of ^{14}Be and ^{17}B. In the numerical output, from which Fig. 11 was constructed, there is a two-dimensional island at the proper place for each nuclide before any tailing subtraction was performed. The net number of events in Figs. 14 and 15 included in the ^{14}Be and ^{17}B peaks are 150 and 50, respectively, clearly above statistical uncertainties where the tailing corrections for these nuclei were 60 and 35 counts, respectively. Both the positions and widths of the peaks are correct for the assignments to ^{14}Be and ^{17}B. Furthermore, although the many windows applied to the data imply stringent conditions, it must be verified that the parameters are reasonably distributed within these windows. Thus, all five of the individual experimental parameters were examined for the new isotopes, as shown in Fig. 18. Those for ^{14}Be are distributed in a manner similar to those for ^{12}Be and those for ^{17}B are similar to ^{15}B. An examination of the tagged pulser events showed that there was no pile-up on the pulser down to a level of 10^{-4} and thus pile-up on to a simulated ^{14}C event does not give rise to any spurious peaks.

The products of the break-up of a metastable nucleus can give rise to spurious peaks of a lower Z isotope in a particle identifier. For example, $^{8}\text{Be} \rightarrow 2\alpha$ identifies as ^{7}Li [31]. Our apparatus, which combines particle identification, time of flight, and pulse width discrimination, is hardly sensitive to this effect. In order for two fragments to be improperly identified as one, both of the fragments from the break-up must enter the small solid angle of the telescope and, in addition, pass through each of the detectors simultaneously. Thus, the center-of-mass motion of the two fragments must be small, both perpendicular and parallel to the detector telescope axis. It can be shown that these requirements set an upper limit of about 10 keV on the Q value for the break-up reaction. The existence of such metastable states is improbable.

Although, in general, relative yields cannot be taken as relative cross sections because of the various experimental discriminations, it was found that for isotopes differing by only two mass numbers, our relative yields at 90° agreed with ratios of the published total production cross sections[24]. For four nuclei for which new cross sections may be estimated, Table IV lists our yield ratios and the corresponding cross sections based on the published values. Other two-mass-number yield ratios (leading to ^{11}Li, ^{12}Be, ^{14}B, and ^{15}B) are in the range of 1/20 to 1/40. Thus, it appears from the ^{14}Be, ^{17}B, and ^{19}C yields that the mass yield curve in this light element region is getting steeper the further one goes from stability. This is in contrast to the results in the Na and K region[10]. However, the sharp decrease in the ^{14}Be yield, which crosses the N = 8 neutron shell, is consistent with the decrease in yield observed at the N = 20 and 28 shells for the very neutron-rich isotopes of Na and K [10].

The particle instability of ^{12}Li and ^{16}B can be established by their absence in Figs. 13 and 15. In addition, the mass resolution of neighboring nuclides is consistent with the absence of ^{12}Li and ^{16}B. Furthermore, when a mass cut at A = 16 is taken, as shown in Fig. 12, the predicted low Z tailing from ^{16}C can explain all events recorded in the ^{16}B mass region.

The instability of ^{13}Li is less certain. There are no counts recorded in the peak region of ^{13}Li, but there is a general background of approximately one event per nuclide in that area of the Z vs. A matrix (see Fig. 19). This gives a limit on the ^{13}Li/^{11}Li ratio of about 1/1400. Although this ratio is smaller than the ^{14}Be/^{12}Be ratio by a factor of 6, the ^{13}Li/^{11}Li ratio is expected to be lower because ^{13}Li is further from beta stability. Therefore, from these data it cannot be concluded that ^{13}Li is particle unstable although the upper limit on the cross section is about 0.2 μb.

A careful investigation of the regions of the Z vs. A matrix for the predicted particle stable nuclei ^{19}B, ^{20}C and ^{22}N was also undertaken and is shown in detail in Fig. 19. Four main criteria were applied to the data to determine whether there was sufficient evidence for their particle stability. These were:

(1) A two-dimensional island should exist in the Z vs. A matrix at the appropriate positions before corrections for tailing.

(2) All experimental data parameters should have the same distributions as known neighboring isotopes.

(3) The net number of events should be three times the statistical error.

(4) The yield should be reasonable based on systematics.

Unfortunately, all three candidates failed at least one of the above criteria. It was therefore concluded that there is insufficient evidence in these data to prove the particle stability of ^{19}B, ^{20}C or ^{22}N. However, the cross section limits for these nuclei can be set at approximately one μb.

V. CONCLUSIONS

This experiment has proven the particle stability of ^{14}Be and ^{17}B, has shown the instability of ^{12}Li and ^{16}B and has confirmed the existence of ^{19}C. In addition, production cross sections have been estimated for four nuclides and approximate upper limits have been set for four others. It was found that in this region of elements the production cross sections fell off more steeply than expected as one went to the limits of particle stability. This present extension of our knowledge of the limits of particle stability was made possible by improvements in apparatus and techniques.

The previous negative result[16] for ^{14}Be was based on a heavy-ion transfer experiment in which the yield was more than a factor of ten lower than that expected from systematics. In that work the log of the cross section was plotted vs. the Q of the reaction calculated for both products in their ground states, and a linear extrapolation was made from the region of measured cross sections. One must conclude that either the linear systematics or the long extrapolation must be questioned.

At the time of our discovery of ^{14}Be it was not realized that the new mass[32] of ^{14}B implied the particle stability[17] of ^{14}Be using the transverse mass relations of Garvey and Kelson. In retrospect, the surprising fact is the mass of ^{14}B which was one MeV lower than that predicted by these mass relations. A recalculation of the mass table taking into account the recent experimental masses of both ^{11}Li [11] and ^{14}B [32] has been prepared[33]. ^{14}Be is predicted to be bound by 0.4 MeV and ^{17}B by 0.5 MeV. ^{12}Li, ^{13}Li, and ^{16}B are predicted to be unbound by 3.9, 4.5, and 1.1 MeV, respectively. In fact, ^{19}C is now predicted to be marginally bound and the only known particle stable nucleus still predicted unbound is ^{32}Na. A recent summary of the situation has been given by Thibault[34].

In order to graphically display the present situation and the future prospects, Fig. 20 has been constructed using the most recent mass predictions[33]. The lightest undiscovered isotope on the neutron excess side of stability is predicted to be ^{19}B and on the neutron deficient side it is ^{20}Mg. Of the heavier elements on the neutron excess side, only oxygen and sodium may be at the limits of particle stability. However, these predictions are based on the Garvey-Kelson relations, and naturally, must be verified experimentally.

ACKNOWLEDGMENTS

We wish particularly to thank Richard Epply for writing the data acquisition program, Don Landis for designing the fast electronics, Fred Goulding for contributing many valuable suggestions, and Jack Walton for fabricating the detectors. Catherine Thibault and Robert Klapisch are to be thanked for discussions which stimulated the experiment, and Nick Jelley for carefully reading the manuscript. The encouragement of Earl K. Hyde and the cooperation of the Bevatron staff are also greatly appreciated.

FOOTNOTES AND REFERENCES

*Research supported by the U. S. Atomic Energy Commission.

†Present address: Los Alamos Scientific Laboratory, Los Alamos, N. M.

‡ Permanent address: Simon Fraser University, Burnaby, B. C., Canada.

‡ Permanent address: Los Alamos Scientific Laboratory, Los Alamos, N. M.

1. S. W. Cosper, J. Cerny, and R. C. Gatti, Phys. Rev. 154, 1193 (1967); J. Cerny, S. W. Cosper, G. W. Butler, R. H. Pehl, F. S. Goulding, D. A. Landis, and C. Detraz, Phys. Rev. Letters 16, 469 (1966).

2. A. M. Poskanzer, R. A. Esterlund, and R. McPherson, Phys. Rev. Letters 15, 1030 (1965).

3. A. M. Poskanzer, P. L. Reeder, and I. Dostrovsky, Phys. Rev. 138, B18 (1965).

4. A. M. Poskanzer, S. W. Cosper, E. K. Hyde, and J. Cerny, Phys. Rev. Letters 17, 1271 (1966).

5. A. M. Poskanzer, G. W. Butler, E. K. Hyde, J. Cerny, D. A. Landis, and F. S. Goulding, Phys. Letters 27B, 414 (1968).

6. T. D. Thomas, G. M. Raisbeck, P. Boerstling, G. T. Garvey, and R. P. Lynch, Phys. Letters 27B, 504 (1968).

7. G. M. Raisbeck, P. Boerstling, P. W. Riesenfeldt, R. Klapisch, T. D. Thomas, and G. T. Garvey in High-Energy Physics and Nuclear Structure, ed. by S. Devons (Plenum, New York (1970)) p. 341.

8. R. Klapisch, C. Philippe, J. Suchorzewska, C. Detraz, and R. Bernas, Phys. Rev. Letters 20, 740 (1968).

9. R. Klapisch, C. Thibault-Philippe, C. Detraz, J. Chaumont, R. Bernas, and E. Beck, Phys. Rev. Letters 23, 652 (1969).

10. R. Klapisch, C. Thibault, A. M. Poskanzer, R. Prieels, C. Rigaud, and E. Roeckl, Phys. Rev. Letters 29, 1254 (1972).

11. R. Klapisch, C. Thibault, C. Rigaud, A. M. Poskanzer, L. Lessard, and W. Reisdorf, to be published.

12. A. G. Artukh, G. F. Gridnev, V. L. Mikheev, and V. V. Volkov, Nucl. Phys. A137, 348 (1969).

13. A. G. Artukh, V. V. Avdeichikov, G. F. Gridnev, V. L. Mikheev, V. V. Volkov, and J. Wilczynski, Phys. Letters 31B, 129 (1970).

14. A. G. Artukh, V. V. Avdeichikov, L. P. Chelnokov, G. F. Gridnev, V. L. Mikheev, V. I. Vakatov, V. V. Volkov, and J. Wilczynski, Phys. Letters 32B, 43 (1970).

15. A. G. Artukh, V. V. Avdeichikov, G. F. Gridnev, V. L. Mikheev, V. V. Volkov, and J. Wilczynski, Nucl. Phys. A176, 284 (1971).

16. A. G. Artukh, V. V. Avdeichikov, J. Ero, G. F. Gridnev, V. L. Mikheev, V. V. Volkov, and J. Wilczynski, Phys. Letters 33B, 407 (1970).

17. A brief report of this work was published as J. D. Bowman, A. M. Poskanzer, R. G. Korteling, and G. W. Butler, Phys. Rev. Letters 31, 614 (1973).

18. G. T. Garvey and I. Kelson, Phys. Rev. Letters 16, 197 (1966).

19. G. T. Garvey, W. J. Gerace, R. L. Jaffe, I. Talmi, and I. Kelson, Rev. Mod. Phys. 41, S1 (1969).

20. J. Cerny in Atomic Masses and Fundamental Constants 4, ed. by J. H. Sanders and A. H. Wapstra (Plenum, New York (1972)) p. 26.

21. G. T. Garvey, Comments on Nuclear and Particle Physics V, 85 (1972).

22. V. V. Volkov, Particles and Nuclei 2, 1 (1973).

23. C. Thibault and R. Klapisch, Phys. Rev. C6, 1509 (1972).

24. A. M. Poskanzer, G. W. Butler, and E. K. Hyde, Phys. Rev. C3, 882 (1971).

25. G. W. Butler, A. M. Poskanzer, and D. A. Landis, Nucl. Instr. Methods 89, 189 (1970).

26. H. Pleyer, B. Kohlmeyer, W. F. W. Schneider, and R. Bock, Nucl. Instr. Methods 96, 263 (1971).

27. B. A. Watson, C. C. Chang, and S. L. Tabor, Particles and Nuclei 2, 376 (1971).

28. A similar device was used by J. Cerny, R. A. Mendelson, G. J. Wozniak, J. E. Esterl, and J. C. Hardy, Phys. Rev. Letters 22, 612 (1969).

29. The small relativistic effect at the highest velocities was adsorbed into the other corrections.

30. S. Datz, C. Erginsoy, G. Leibfried, and H. O. Lutz, Ann. Rev. Nucl. Sci. 17, 129 (1967).

31. G. J. Wozniak, H. L. Harney, K. H. Wilcox, and J. Cerny, Phys. Rev. Letters 28, 1278 (1972).

32. G. C. Ball, G. J. Costa, W. G. Davies, J. S. Forster, J. C. Hardy, and A. B. McDonald, Phys. Rev. Letters 31, 395 (1973).

33. C. Thibault and R. Klapisch, private communication (1973).

34. C. Thibault, J. de Physique, to be published.

APPENDIX A

Pulse Width Discrimination Theory

The principle of our pulse width discriminator is to measure the width of each shaped detector pulse from leading edge to cross-over. A block diagram of the apparatus with illustrative wave forms is given in Fig. 21. Wave forms 1, 2 and 3 represent an unperturbed event and events perturbed by a small pulse coming early and late, respectively. The time delay between the main and perturbing pulses is large compared to the intrinsic resolution of the instrument. The wave forms illustrate an asymmetry in the operation of the PWD in this time region: a small perturbing pulse coming early alters greatly the time of the leading edge discriminator while the cross-over time signal is affected to the same extent for both early and late perturbing pulses. Thus, it appears that this apparatus is more effective in detecting the presence of small perturbing pulses coming early than coming late. However, in order to determine the pulse pair resolution it is necessary to describe the response to two pulses which come at nearly the same time and not widely separated, and easily rejected in any case, as illustrated in Fig. 21. It will be shown that this pulse pair resolution is proportional to the spread in the charge deposition profile relative to that of a single event and is not sensitive to the time order of the two events. Thus, although a leading-edge to cross-over discriminator is equally effective for small pulses coming early or late, a leading-edge to trailing-edge discriminator would be more effective, but not as dramatically as one would believe based on the long time scale arguments.

Suppose that two ions impinge on the detector at times t_1 and t_2. For what values of $t_2 - t_1$ will the PWD output differ significantly from the output

produced by a single event? For a single event which impinges on the detector at time t_o we assume that the unipolar output rises like a power of time, at least until the discriminator level is reached:

$$V = Ht^q \tag{1}$$

where V is the output voltage,

H is a factor proportional to the amplitude, E or ΔE, of the pulse,

t is time, and

q is a dimensionless number characteristic of the electronics.

We assume that timing variations due to the cross-over trigger may be neglected since the velocity of the cross-over is large compared to the velocity at the leading edge.

If two ions strike the detector at times t_1 and t_2 having relative amplitudes H_1 and H_2, the unipolar output voltage will then be

$$V = H_1(t - t_1)^q + H_2(t - t_2)^q \quad . \tag{2}$$

Since we are interested in events of a unique amplitude we set

$$H_1 + H_2 = H \tag{3}$$

and, for convenience, we define the zero of time by

$$H_1t_1 + H_2t_2 = 0 \quad . \tag{4}$$

Thus, the cross-over discriminator will trigger as if the pulse resulted from a single event. Let w be the level of the leading edge discriminator and y and y' be the times at which it will fire for single and double events,

$$w = Hy^q \tag{5}$$

and

$$w = H_1(y' - t_1)^q + H_2(y' - t_2)^q \quad . \tag{6}$$

Equation (6) which defines y' may be expanded in a Taylor series assuming t_1, $t_2 \ll y'$. When the resulting equation is truncated and combined with (5) the solution is

$$y - y' = \frac{q - 1}{2y} \left\{ \frac{H_1}{H} t_1^2 + \frac{H_2}{H} t_2^2 \right\} \quad . \tag{7}$$

The quantity in brackets is the mean square time spread of the charge deposition. We determined the width of the acceptance window Δt by the points on the single event peak at one quarter of its maximum amplitude. To obtain the pulse pair resolution of the PWD defined by 50% rejection of two nearly overlapping signals we set

$$y - y' = \Delta t/2 \tag{8}$$

and solve the resulting equation for $t_2 - t_1$:

$$t_2 - t_1 = \sqrt{\frac{H}{H_1} \frac{H}{H_2} \frac{y\Delta t}{q - 1}} \quad . \tag{9}$$

From the structure of this equation we see that the pulse pair resolution depends on the amplitude ratio of the two pulses which are piled up. The apparatus has the best resolution when the two pulses have equal amplitude,

but if one pulse is ten times smaller than the other the resolution is worse only by the factor 1.7. Of course, if the amplitude ratio is very large, the assumption that the small pulse is rising as t^q will no longer hold. We now discuss the determination of q and y, and the related problem of the walk of the PWD output with amplitude.

Since the cross-over timing is independent of amplitude, the amplitude dependence of the PWD output is given by relation (5), which may be solved to yield

$$y = \left(\frac{w}{H}\right)^{1/q} . \qquad (10)$$

As described in Section IIID scatter plots of y vs. $\mathcal{E}^{-1/q}$ were made from the data for various values of q. It was found that a linear relationship was obtained for q = 3. An integral value of q for the initial rise of the pulse would be predicted if the detector-preamplifier-amplifier circuit is describable in terms of multiple RC integrators. The value of y was read off the straight line and the pulse pair resolution was then calculated for equal amplitude pulses. Table V summarizes these results.

APPENDIX B

Determination of ΔE Detector Thickness Uniformity

A one mm^2 ^{241}Am alpha source (5.48 MeV) was placed 2.5 cm from a 4 × 6 mm Si(P) detector. The wafers to be tested were placed as absorbers between the alpha source and the detector. Two alpha-energy spectra were recorded for each wafer, one with the wafer near the source and the other with the wafer near the detector. The former geometry illuminates only a small central spot of the wafer and the latter illuminates a 4 × 6 mm area. If we assume that the thickness inhomogeneity of the small spot is negligible, then a comparison of the line widths in the two geometries gives the inhomogeneity of the wafer. Range energy relations were used to deduce the wafer thickness from the energy of the transmitted alphas and to relate the change in line width to the thickness inhomogeneity. The FWHM variation in detector thickness is given by

$$\Delta x = \sqrt{W_2^2 - W_1^2} \Big/ (dE/dx)$$

where dE/dx is the specific energy loss at the degraded alpha energy, and W_2 and W_1 are the alpha line widths (FWHM) in the two geometries. The detector used in this experiment, which had a thickness of 24 μm, had a Δx of 1.0 μm.

APPENDIX C

The Mass Dependence of PI

When c = 0 our PI algorithm (Eq. (8) of Section IIIC) reduces to the square root of the algorithm first introduced by Goulding and Landis, and has the value

$$PI \propto \sqrt{x/a(Z,A)} \quad . \tag{1}$$

The quantity x is the ΔE detector thickness and a(Z,A) is the constant entering in the approximate range-energy relation

$$R = a(Z,A)\, E^{b} \quad . \tag{2}$$

Since the specific energy loss depends only on the nuclear charge Z and the velocity of the ion v we can write

$$\frac{dE}{dx} = f(Z,v) \quad . \tag{3}$$

Expression (2) may be differentiated to obtain

$$\frac{dE}{dx} = \frac{1}{abE^{b-1}} \quad , \tag{4}$$

which when combined with (3) yields

$$a \propto A^{-(b-1)} \quad . \tag{5}$$

By substituting this into (1) we expect the expression

$$PI/A^{(b-1)/2} \tag{6}$$

to be approximately independent of mass and to be a function of nuclear charge only. From the Bethe-Bloch expression for dE/dx one expects that (6) will be linearly proportional to nuclear charge. Inspection of Fig. 6(b) shows this to be approximately true.

Table I. Detector Characteristics

	ΔE	E
Thickness (μm)	24	67
10-90% rise time for alphas (nsec)	1.9	2.7
10-90% rise time for pulser (nsec)	2.2	3.0
Bias (V)	100	190
Minimum field (V/μm)	3.8	2.6
Temperature (°C)	-21	-25

Table II. Parameters for the Time-of-Flight Analysis

	Symbol	Value
Dead layer on front of the E detector (mg/cm^2)	δx	0.14
Power in the range-energy equation	b	1.6
Coefficient of walk with range ($psec/mg/cm^2$)	ϕ	8.5
Coefficient of walk with ΔE (psec/MeV)	ε	7.5
Time resolution for ^{11}B (psec)	FWHM	290
Time resolution for pulser (psec)	FWHM	100

Table III. Parameters of the Pulse-Width-Discriminator Analysis

	Symbol	Value	
		ΔE	E
Power of walk with energy	-1/q	-1/3	-1/3
Coefficient of walk with energy (nsec-MeV$^{1/3}$)	β	3.8	3.6
Coefficient of walk with range (psec/mg/cm^2)	γ	---	11
Time resolution for ^{11}B (psec)	FWHM	140 (14 MeV)	70 (20 MeV)
Time resolution for pulser (psec)	FWHM	115	60
Acceptance window (psec)	FW$\frac{1}{4}$M	200	90

Table IV. Yield Ratios, A/(A-2), and Production Cross Sections

A_Z	Yield Ratio	$\sigma(\mu b)$
$^{14}_{Be}$	1/225	$\approx$ 10
$^{17}_{B}$	1/100	$\approx$ 5
$^{18}_{C}$	1/20	$\approx$ 100
$^{19}_{C}$	1/60	$\approx$ 5

Table V. Pulse Pair Resolution of the Pulse Width Discriminators

	Symbol	Value	
		ΔE	E
Acceptance window (psec)	Δt	200	90
Discriminator level (MeV)	w	0.3	0.4
Power of time	q	3	3
Trigger time (nsec)	y	1.5 (14 MeV)	1.4 (20 MeV)
Pulse pair resolving time (psec)	t_2-t_1	770	500

FIGURE CAPTIONS

Fig. 1. Schematic diagram of the electronics. The following abbreviations have been used: PWD is pulse width discriminator; C/O is cross-over discriminator; TAC is time-to-amplitude converter; PI is particle identifier; SCA is single channel analyzer; and PUR is pile-up rejector.

Fig. 2. Contour plots of calculated T_{zero} vs. calculated time of flight for boron isotopes with an assumed mass of 11. The lowest contour is at the 5 count level and there are two logarithmically-spaced contour levels per decade. The data in Figs. 2-10 are representative of 4.5×10^5 events of Li through N, or 3.6% of the total amount of data recorded for this experiment. Dead layer and walk with range corrections have been applied in (b) but not in (a). Note in (b) the extrapolation of all the isotopes to a common T_{zero} at zero flight time.

Fig. 3. Histogram of calculated T_{zero} for boron isotopes with an assumed mass of 11. This figure shows only those events that deposited from 18 to 22 MeV in the E detector.

Fig. 4. Contour plot of ΔE vs. E. The banana-shaped ridges correspond to the elements Li through N. The rectangular shape of the plot is caused by the ΔE and E single channel analyzers. The lower right corner is cut off because these particles penetrate the E detector and are rejected by the veto detector. The lowest contour is at the one count level and there are two logarithmically-spaced contour levels per decade.

Fig. 5. Contour plot of E vs. particle identification signal (PI). The lowest contour is at the 5 count level.

Fig. 6. Histograms of (a) particle identification signal (PI), and (b) calculated nuclear charge (Z).

Fig. 7. Contour plots of (a) E pulse-width-discriminator (EPWD) signal vs. E and (b) normalized E pulse-width-discriminator (NEPWD) signal vs. E for Li through N fragments. The acceptance region for the final data analysis is shown in (b). The lowest contour is at the 5 count level in both plots. In (b) the vertical scale has been expanded by a factor of five.

Fig. 8. Histogram of normalized E pulse-width-discriminator (NEPWD) signal, showing the acceptance window that was used in the final data analysis.

Fig. 9. Contour plots of nuclear charge (Z) vs. mass number (A) for a small part of the data (a) without and (b) with the pulse-width-discriminator windows applied. The lowest contour is at the one count level.

Fig. 10. Contour plot of normalized E pulse-width-discriminator (NEPWD) signal vs. E for events falling in the high mass background region of Fig. 9a. Compare with Fig. 7(b). The lowest contour is at the one count level.

Fig. 11. Contour plot of nuclear charge (Z) vs. mass number (A) constructed from all of the data. The lowest contour is at the 3 count level and there are two logarithmically-spaced contour levels per decade.

Fig. 12. Graph showing the determination of the extent of tailing to Z - 1 in the nuclear charge spectrum. The abscissa has been normalized to Be (Z = 4) and the ^{13}B data have been normalized to the ^{10}Be data in intensity. The average of the smooth curves drawn through the ^{10}Be and ^{13}B data points was used to calculate the predicted shape of the ^{16}C curve, and it was normalized to the ^{16}C data for comparison.

Fig. 13. Mass yield spectrum for lithium isotopes. In Figs. 13-17 both zero and one count levels are shown for clarity, and the arrows for the new and missing isotopes point to the expected positions of the peaks based on the positions of the main isotopes.

Fig. 14. Mass yield spectrum for beryllium isotopes.

Fig. 15. Mass yield spectrum for boron isotopes.

Fig. 16. Mass yield spectrum for carbon isotopes.

Fig. 17. Mass yield spectrum for nitrogen isotopes.

Fig. 18. Distribution of raw data parameters for (a) ^{14}Be and (b) ^{17}B. The smooth curves for ^{12}Be and ^{15}B have been approximately scaled to match the histograms.

Fig. 19. Enlarged sections of several high mass regions of the two parameter nuclear charge (Z) vs. mass number (A) plot. The numbers represent counts and the areas are shaded for more than 9 counts. The inner enclosed areas show the predicted locations of the indicated high mass nuclides.

Fig. 20. Low Z region of the chart of the nuclides. Enclosed in boxes are those nuclei predicted to be particle stable.[33] Nuclei known to exist are shaded. Nuclei which have been shown experimentally to be unbound with respect to nucleon emission are indicated by an X. This figure was constructed in collaboration with J. Cerny.

Fig. 21. Pulse width discriminator block diagram. Wave forms labeled "Good" are from a single event. Wave forms labeled "Bad" illustrate two ions passing through the detector separated by about one rise time.

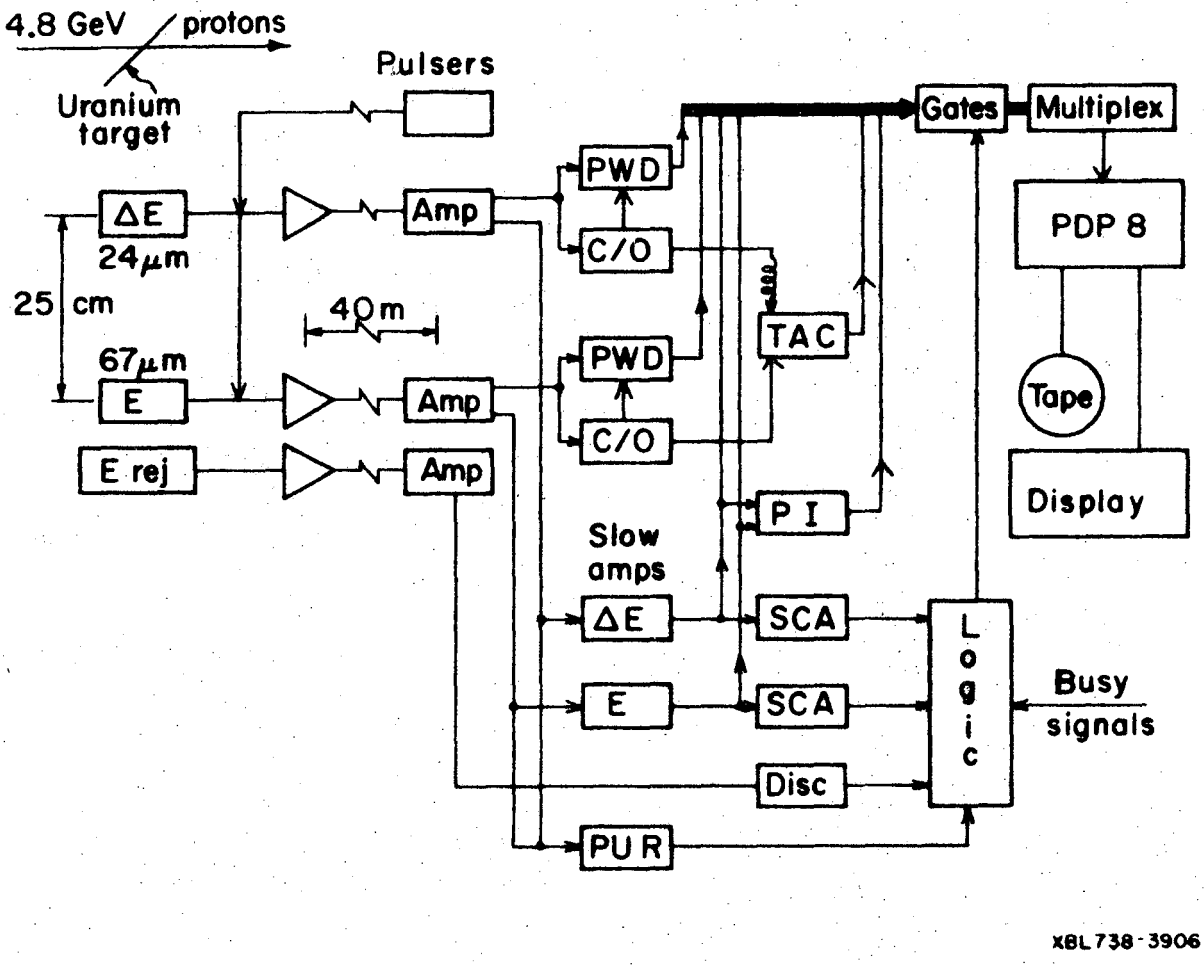
4.8 GeV protons
Uranium target
Pulsers
ΔE
24μm
25 cm
40m
67μm
E
E rej
Amp
Amp
Amp
PWD
C/O
PWD
C/O
TAC
PI
Slow amps
ΔE
E
SCA
SCA
Disc
PUR
Gates
Multiplex
PDP 8
Tape
Display
Logic
Busy signals
XBL738-3906

Fig. 1

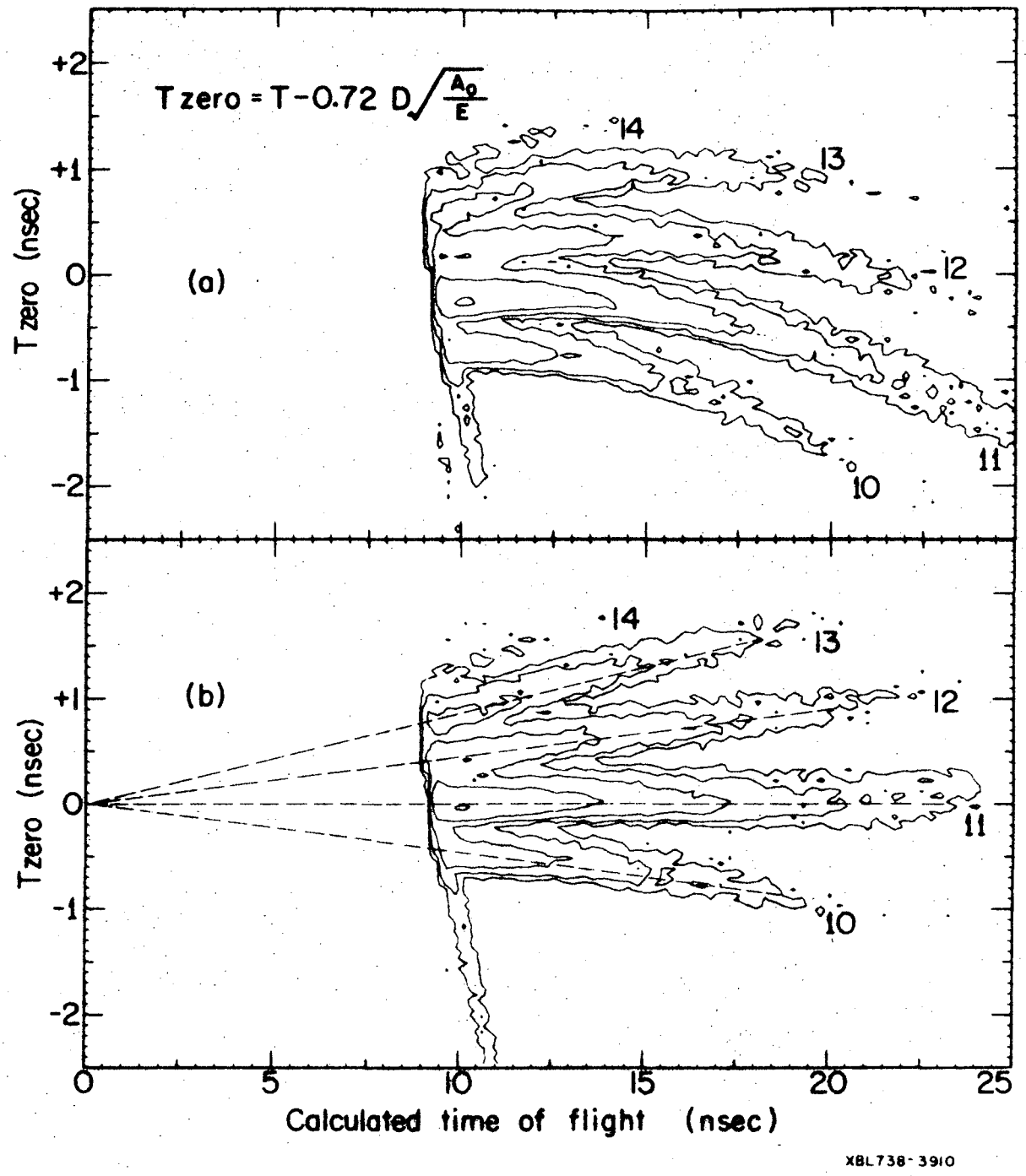
T zero = T - 0.72 D √(A0/E)
(a)
(b)
T zero (nsec)
+2
+1
0
-1
-2
14
13
12
11
10
0
5
10
15
20
25
Calculated time of flight (nsec)
XBL738-3910

Fig. 2

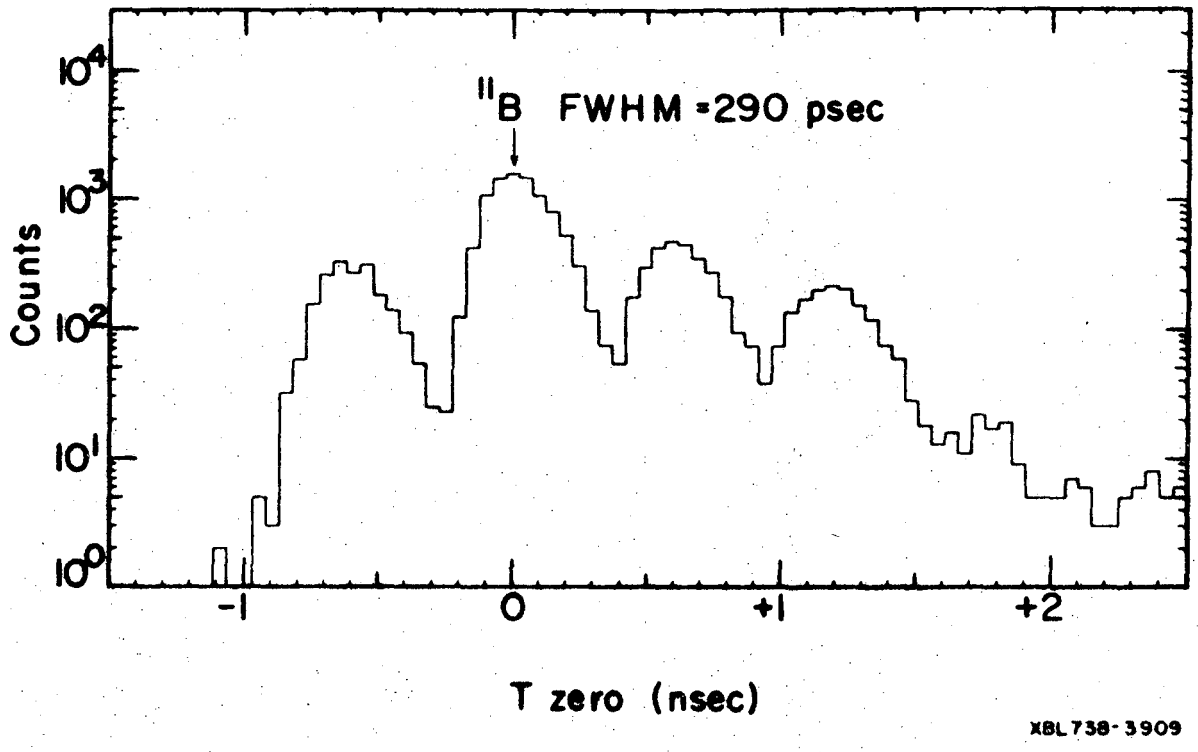
^{11}B FWHM =290 psec
Counts
10^4
10^3
10^2
10^1
10^0
-1
0
+1
+2
T zero (nsec)
XBL738-3909

Fig. 3

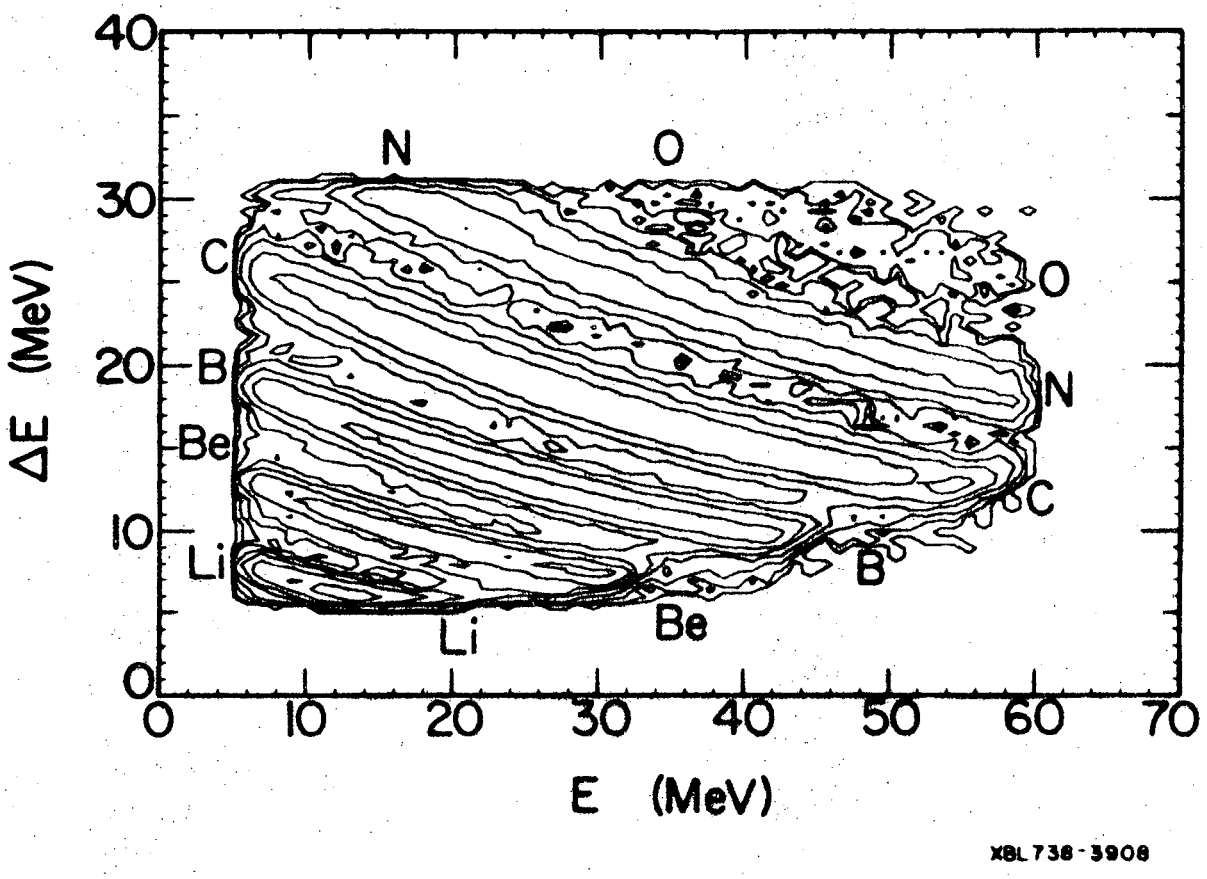
40
30
20
10
0
ΔE (MeV)
0
10
20
30
40
50
60
70
E (MeV)
N
O
C
O
B
N
Be
C
Li
B
Li
Be
XBL 738-3908

Fig. 4

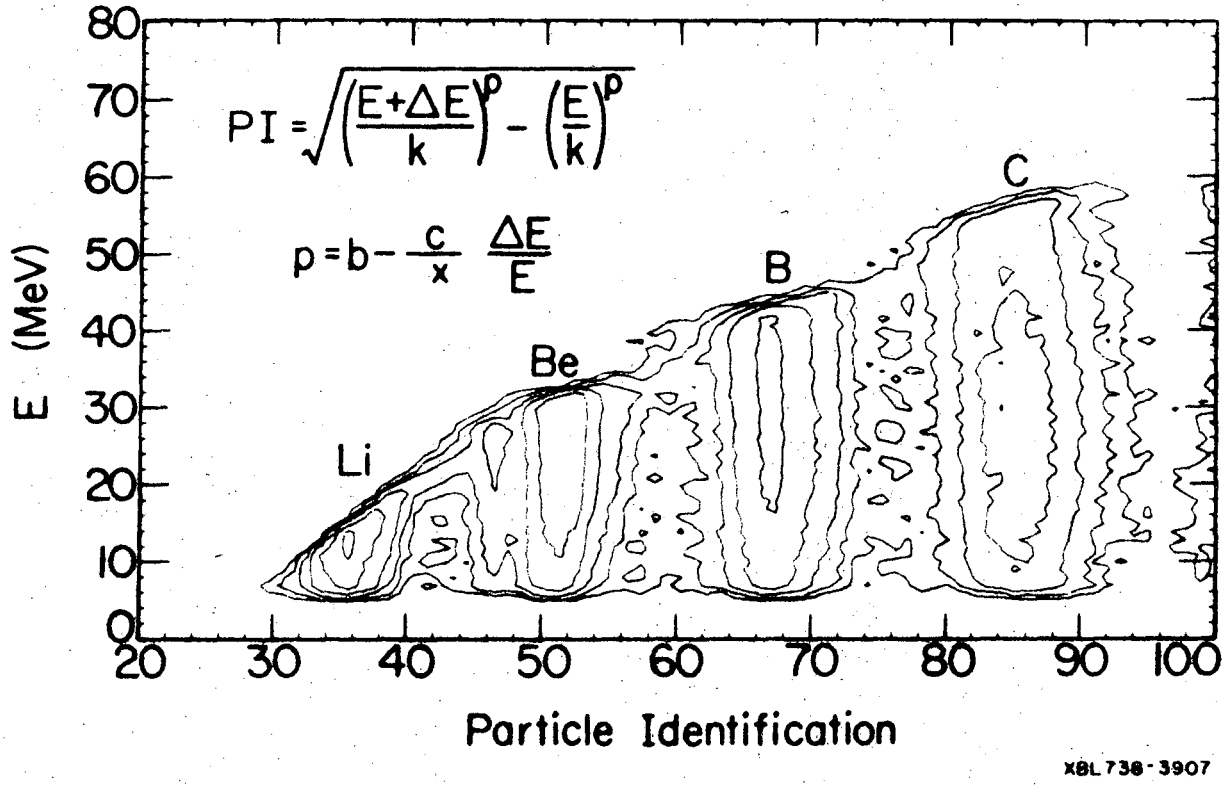
$PI = \sqrt{\left(\frac{E+\Delta E}{k}\right)^p - \left(\frac{E}{k}\right)^p}$
$p = b - \frac{c}{x}\frac{\Delta E}{E}$
Li
Be
B
C
E (MeV)
Particle Identification
0
10
20
30
40
50
60
70
80
20
30
40
50
60
70
80
90
100
XBL738-3907

Fig. 5

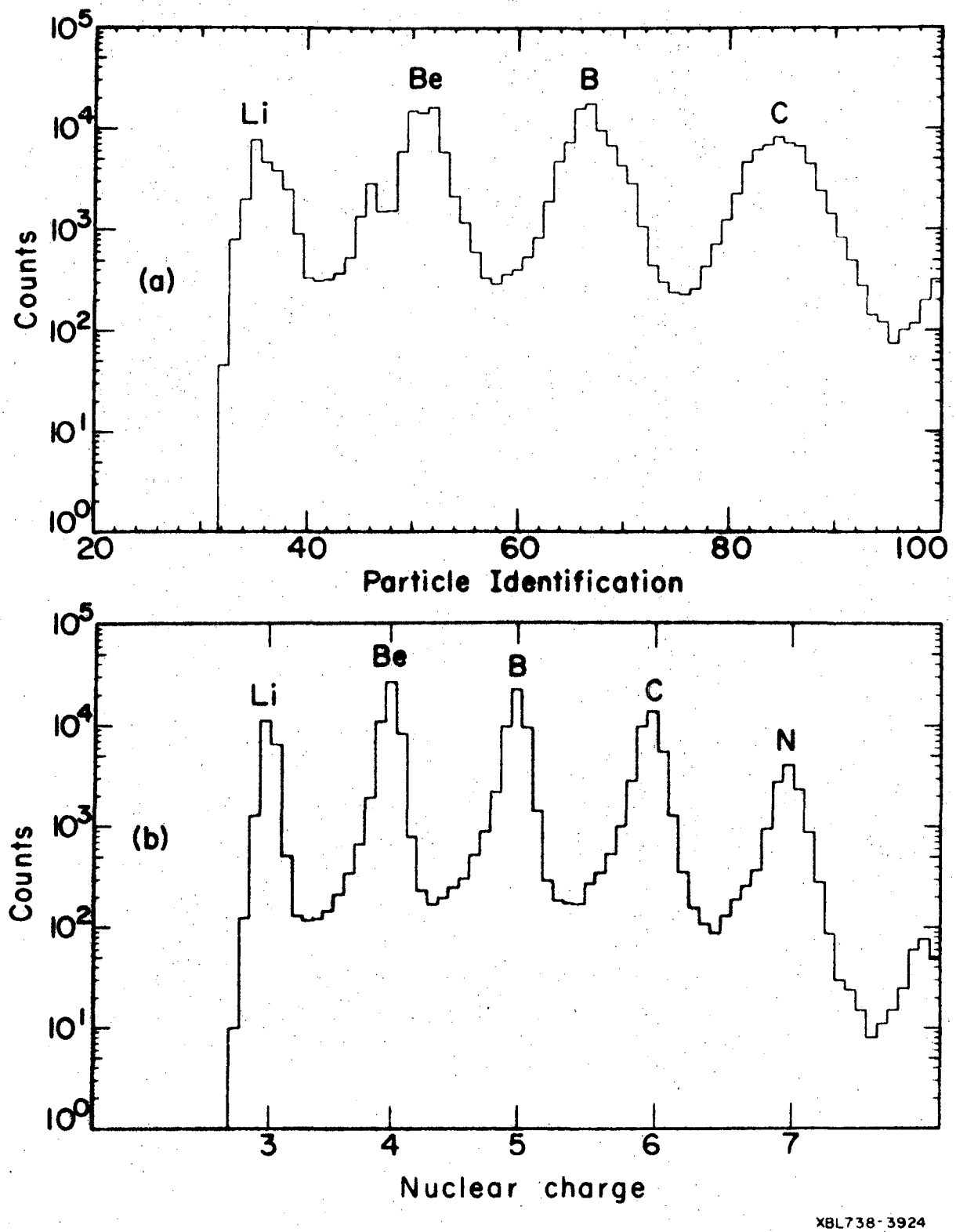
Counts
(a)
Li
Be
B
C
Particle Identification
(b)
Li
Be
B
C
N
Nuclear charge
XBL738-3924

Fig. 6

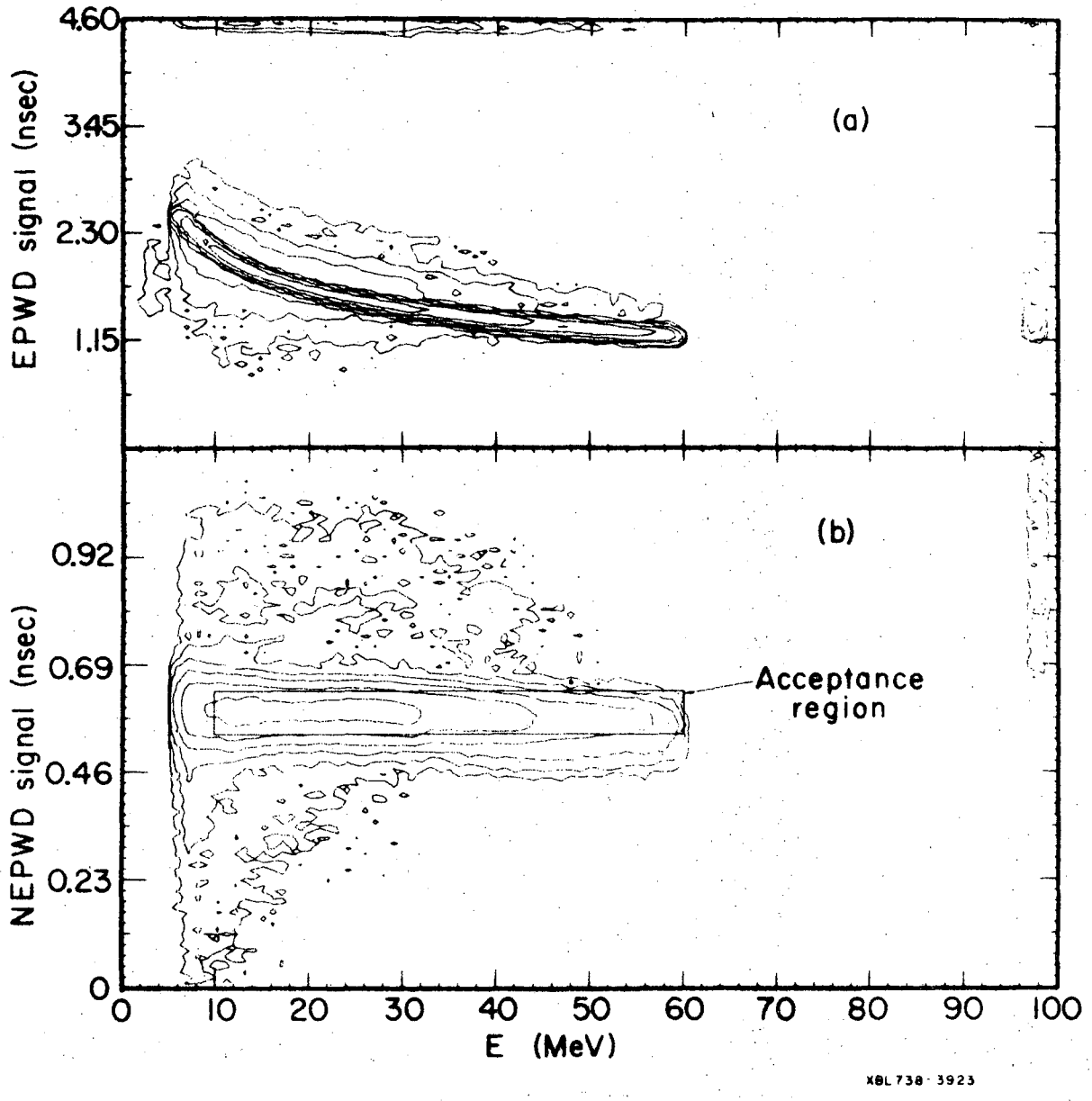
4.60
3.45
2.30
1.15
EPWD signal (nsec)
(a)
0.92
0.69
0.46
0.23
0
NEPWD signal (nsec)
(b)
Acceptance region
0
10
20
30
40
50
60
70
80
90
100
E (MeV)
XBL 738-3923

Fig. 7

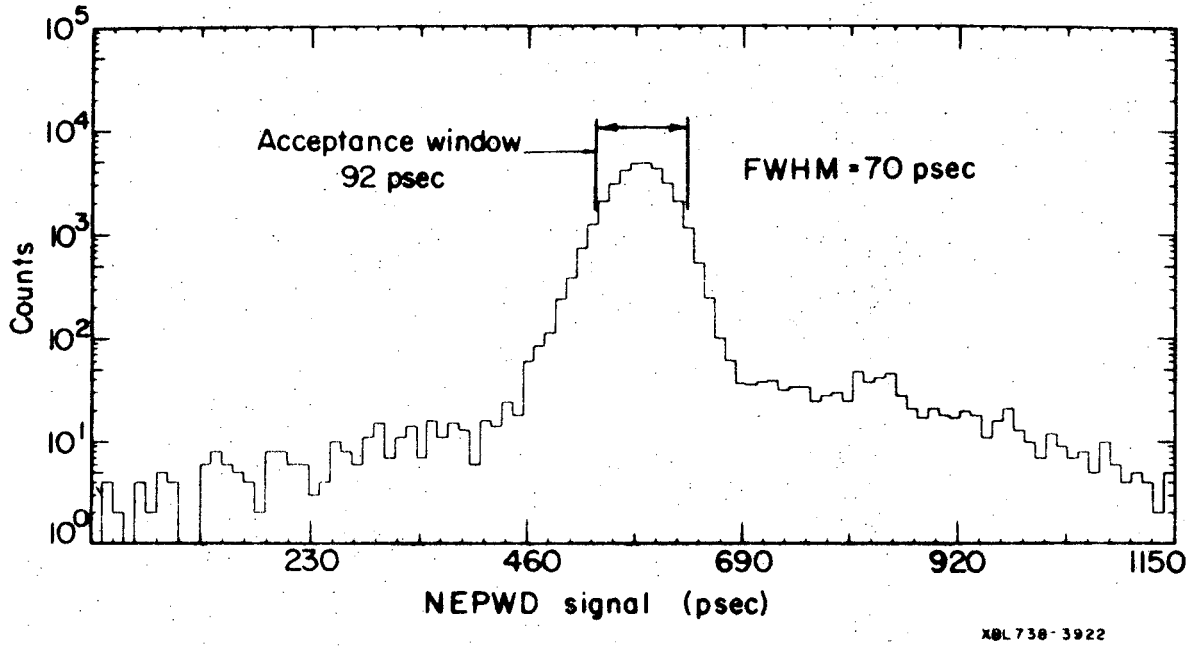
Acceptance window
92 psec
FWHM = 70 psec
Counts
NEPWD signal (psec)
XBL 738-3922

Fig. 8

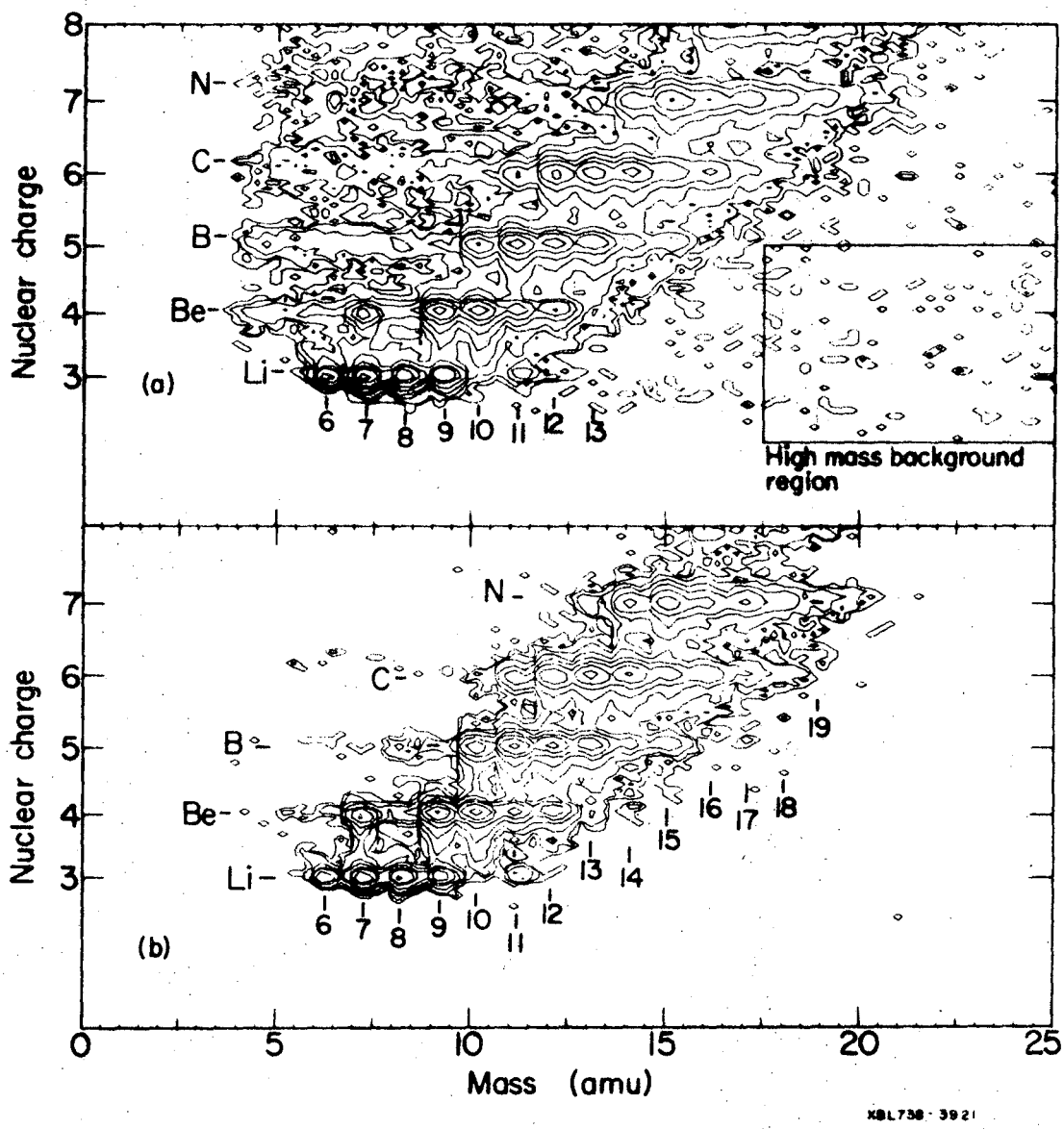
Nuclear charge
Mass (amu)
(a)
(b)
N
C
B
Be
Li
High mass background region
XBL738-3921

Fig. 9

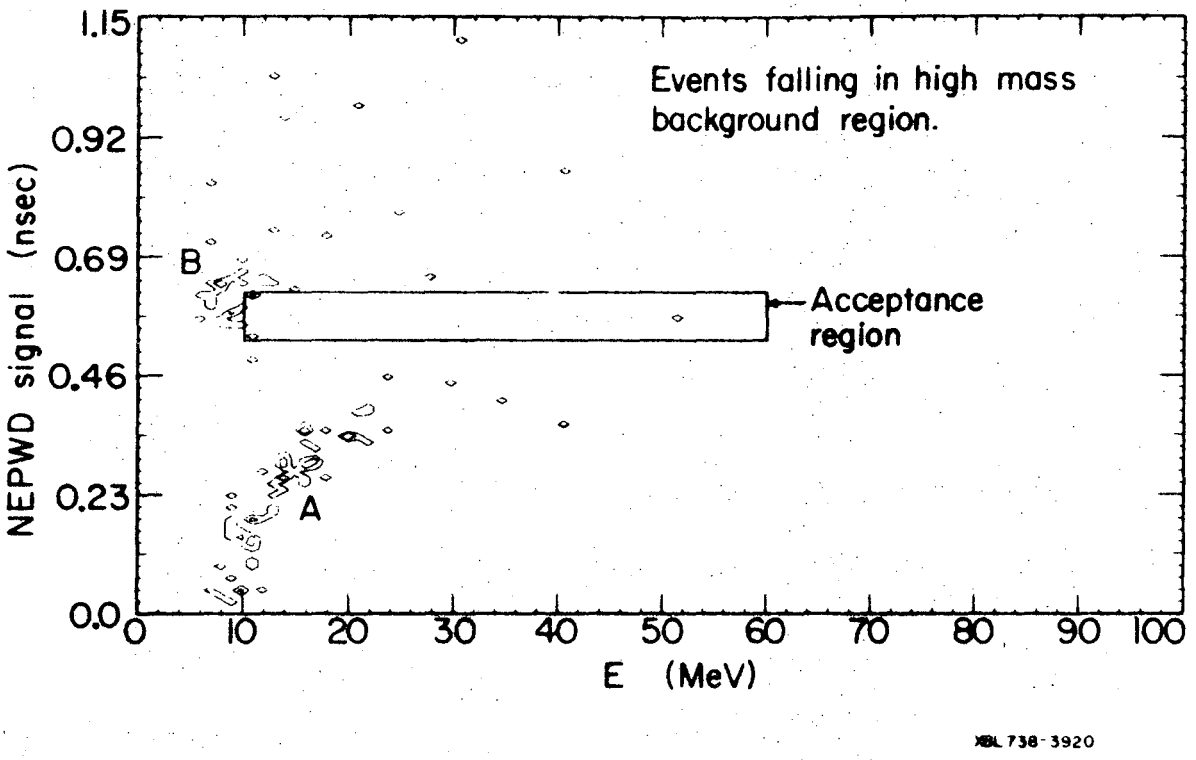
1.15
0.92
0.69
0.46
0.23
0.0
NEPWD signal (nsec)
Events falling in high mass background region.
B
Acceptance region
A
0
10
20
30
40
50
60
70
80
90
100
E (MeV)
XBL 738-3920

Fig. 10

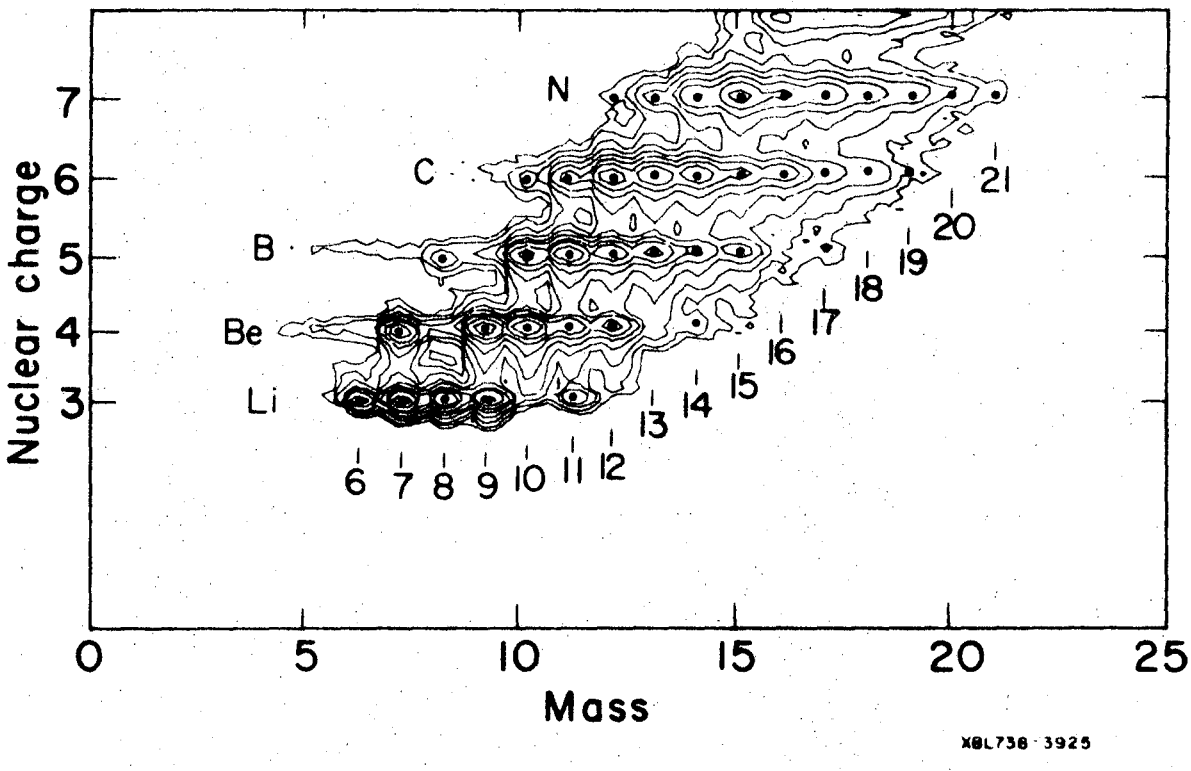
Nuclear charge
Mass
N
C
B
Be
Li
7
6
5
4
3
0
5
10
15
20
25
6 7 8 9 10 11 12
13 14 15 16 17 18 19 20 21
XBL738-3925

Fig. 11

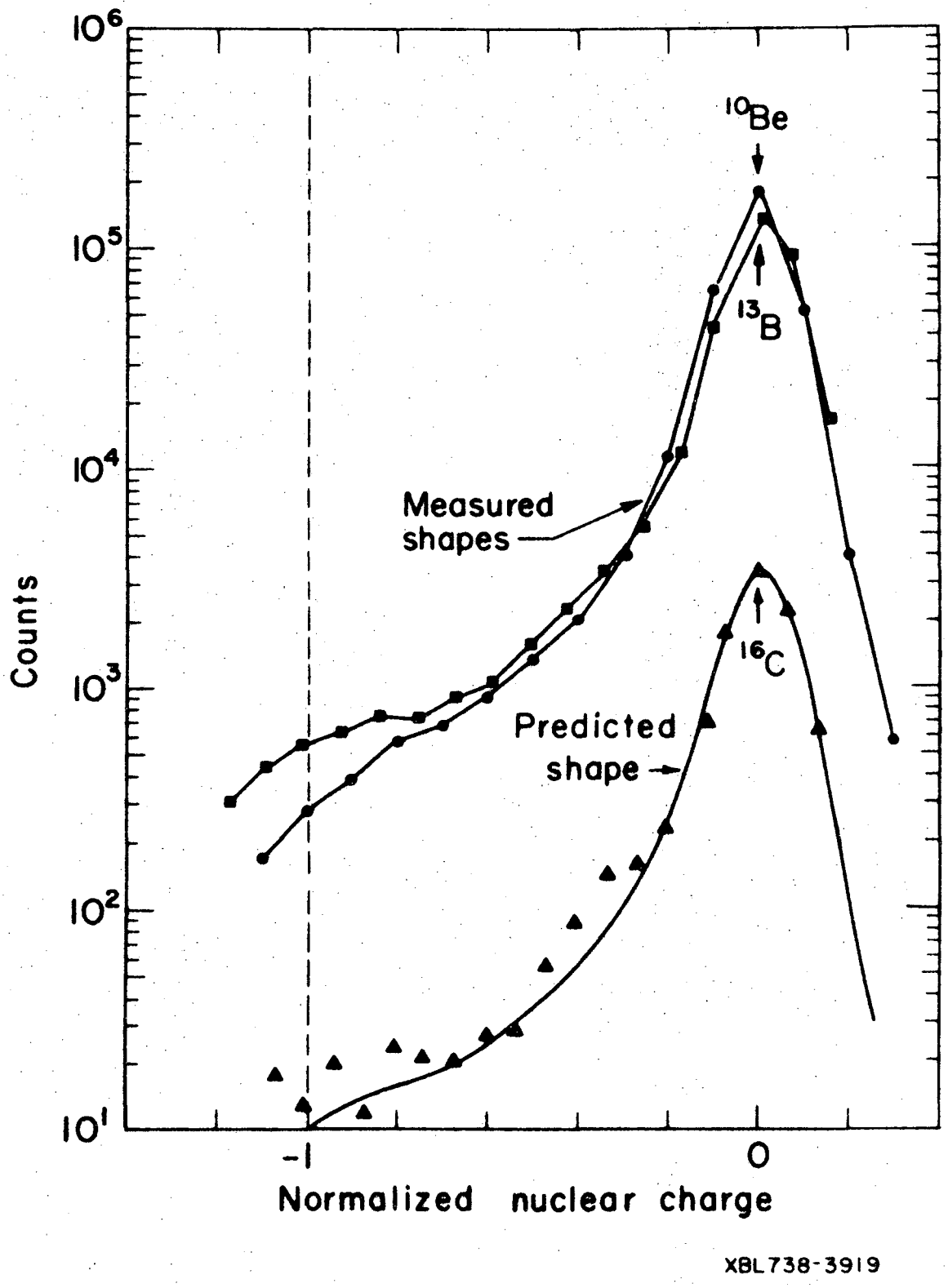
10^6
10^5
10^4
10^3
10^2
10^1
Counts
^{10}Be
^{13}B
Measured shapes
^{16}C
Predicted shape
-1
0
Normalized nuclear charge
XBL738-3919

Fig. 12

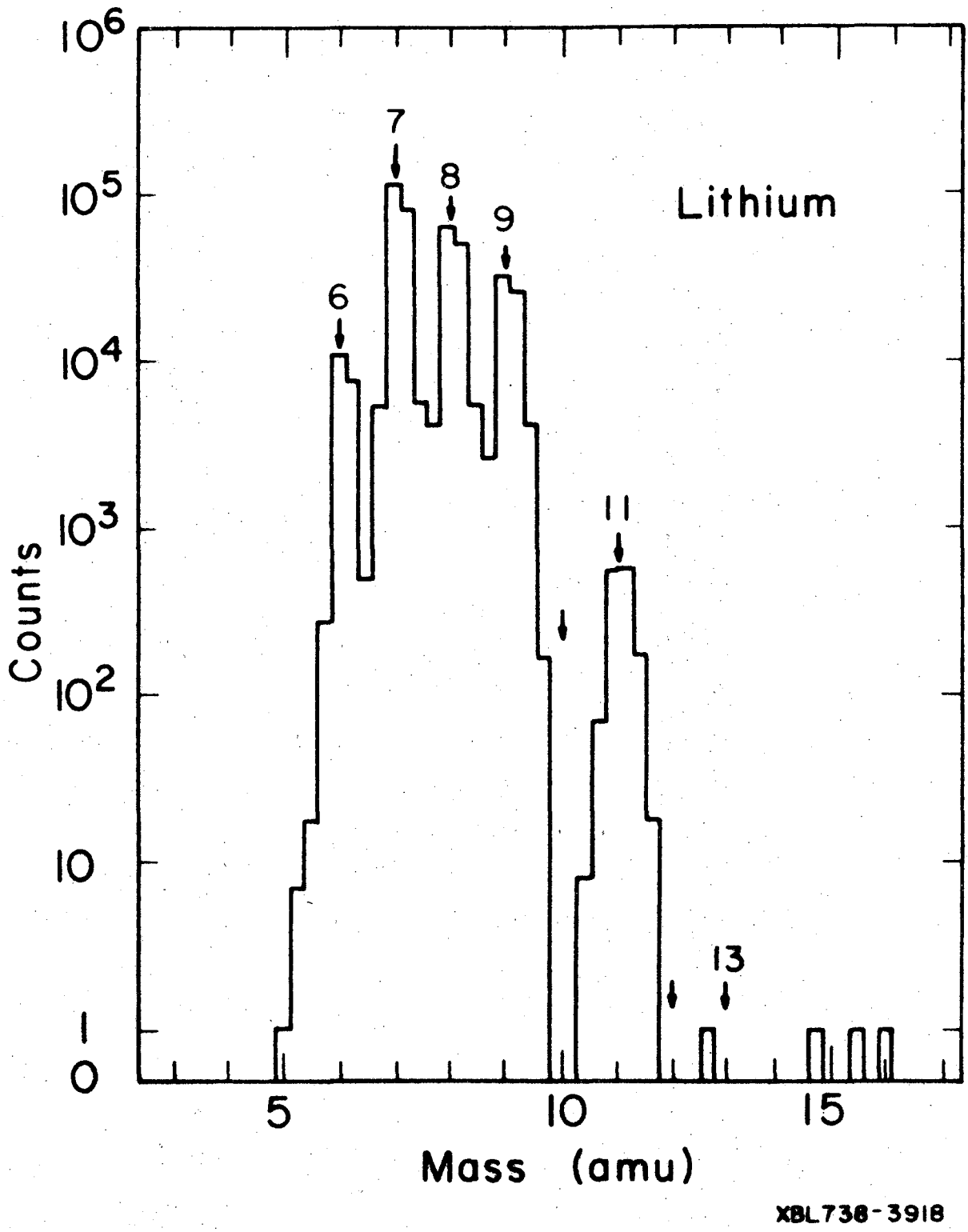

Fig. 13

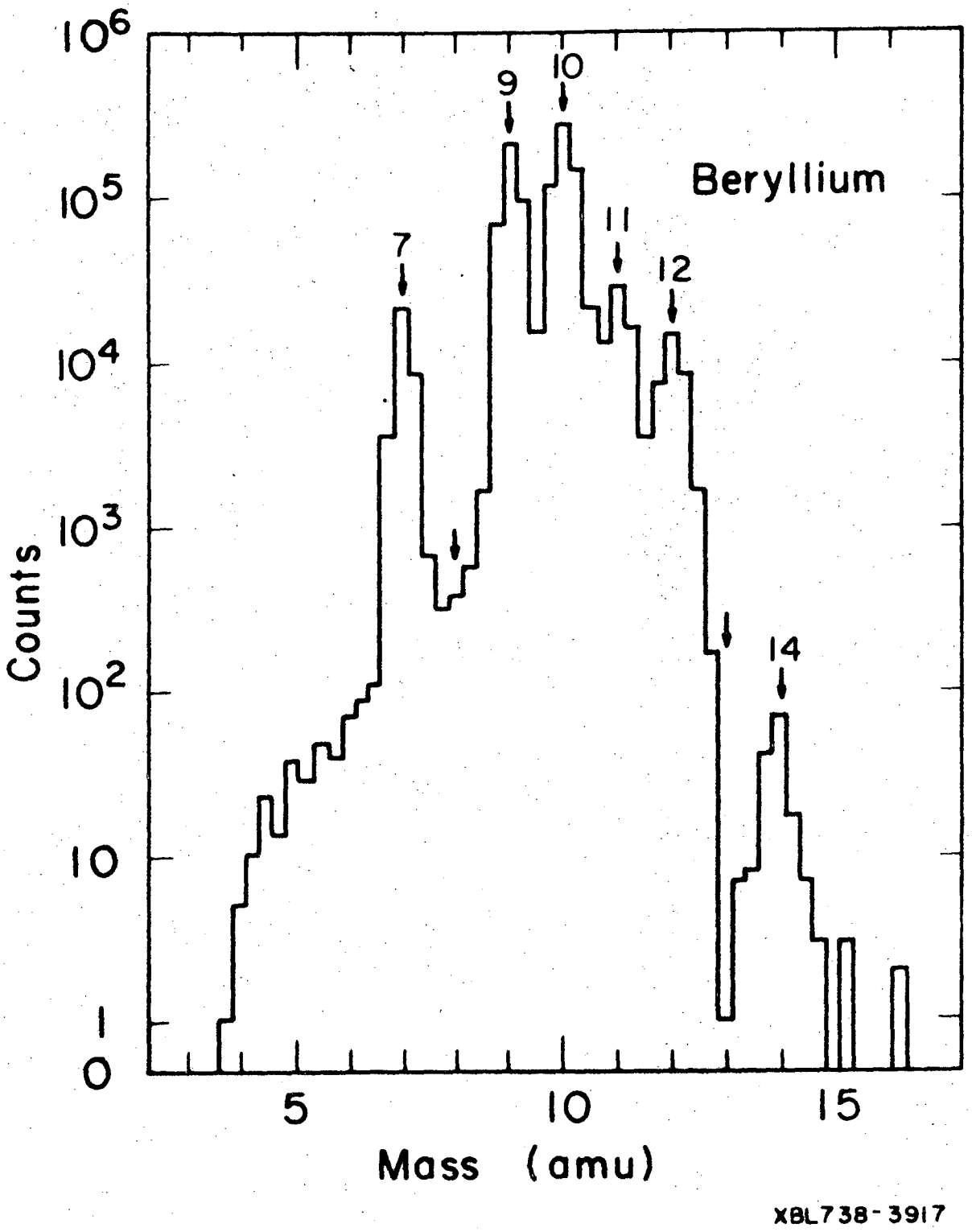

Fig. 14

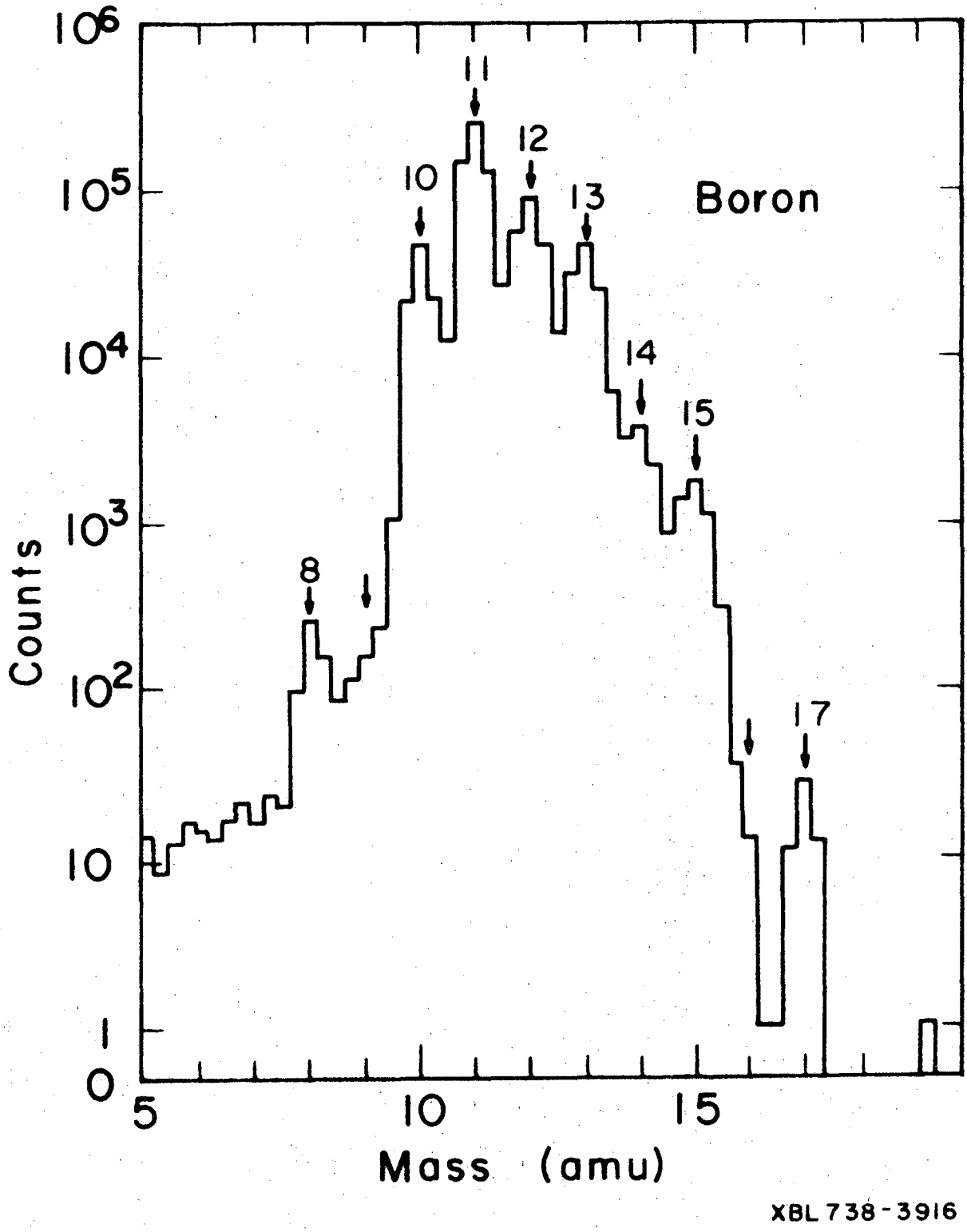
Boron
Counts
Mass (amu)
10^6
10^5
10^4
10^3
10^2
10
1
0
5
10
15
8
10
11
12
13
14
15
17
XBL 738-3916

Fig. 15

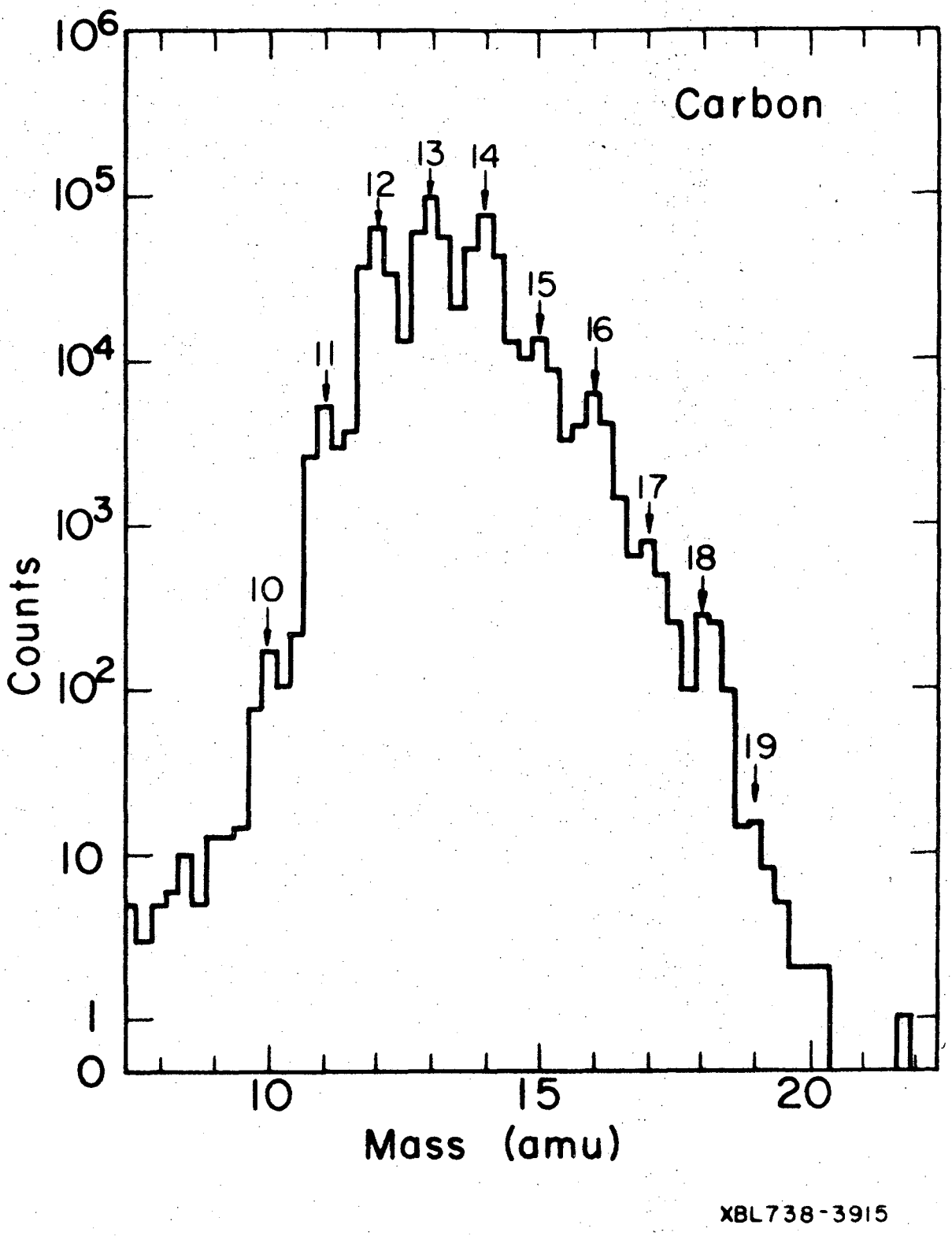
Carbon
Counts
Mass (amu)
10
15
20
0
1
10
10^2
10^3
10^4
10^5
10^6
10
11
12
13
14
15
16
17
18
19
XBL738-3915

Fig. 16

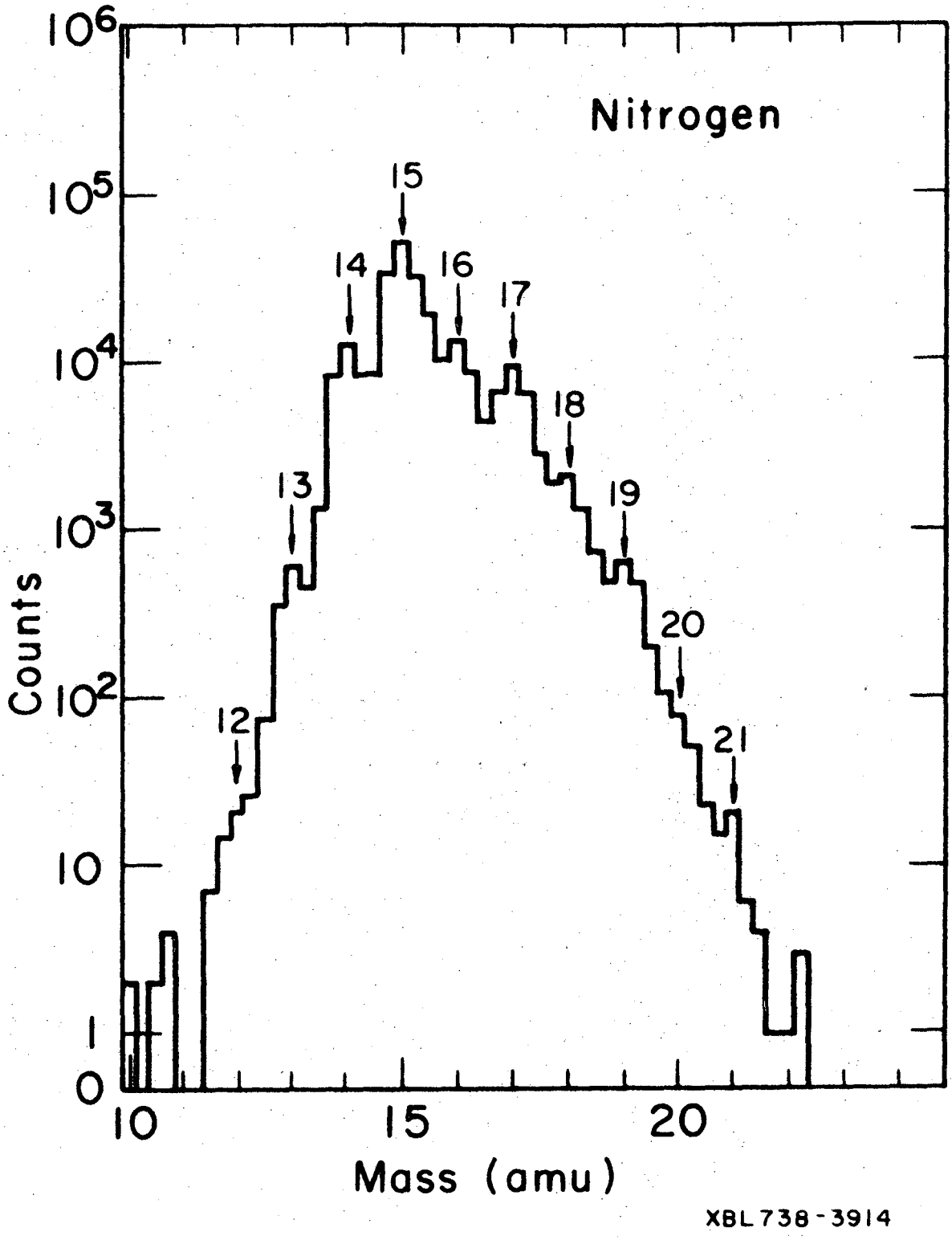
Nitrogen
Counts
Mass (amu)
10⁶
10⁵
10⁴
10³
10²
10
1
0
10
15
20
12
13
14
15
16
17
18
19
20
21
XBL738-3914

Fig. 17

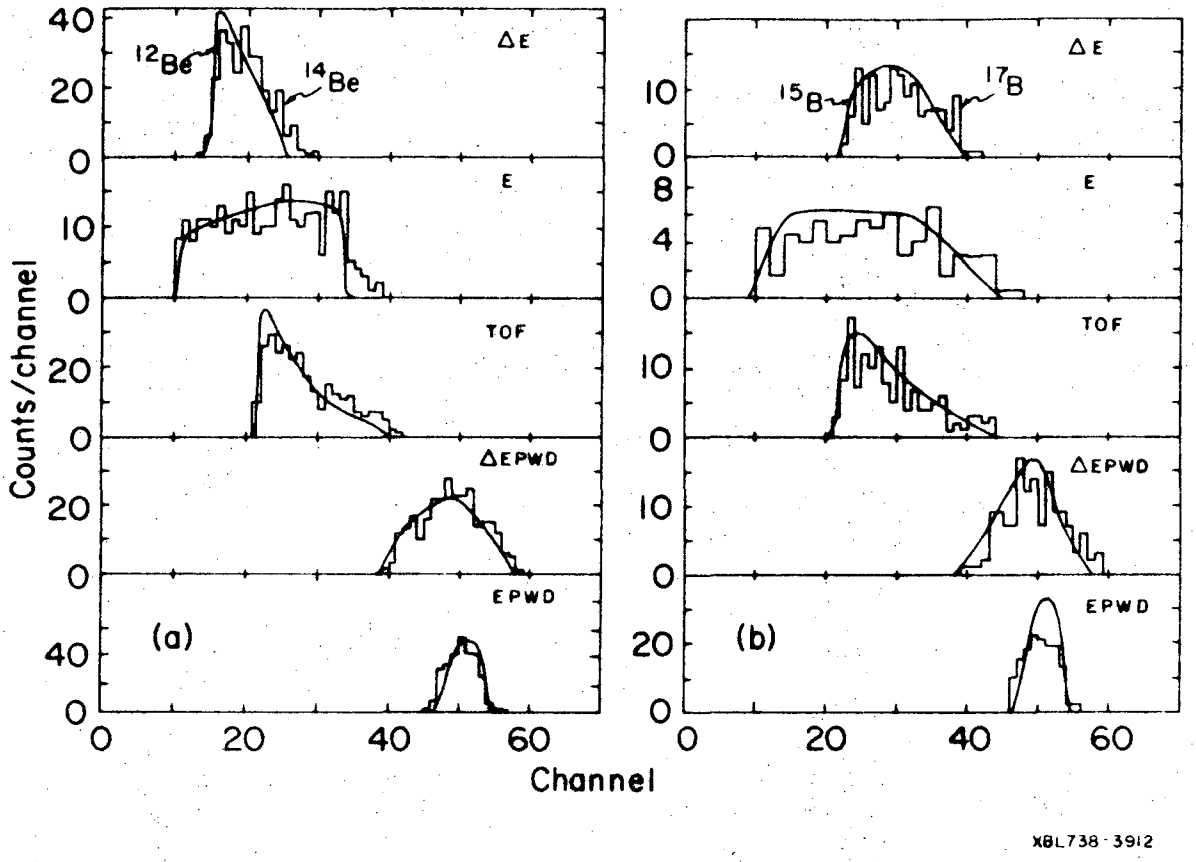
ΔE
E
TOF
ΔEPWD
EPWD
^{12}Be
^{14}Be
^{15}B
^{17}B
(a)
(b)
Counts/channel
Channel
XBL738-3912

Fig. 18

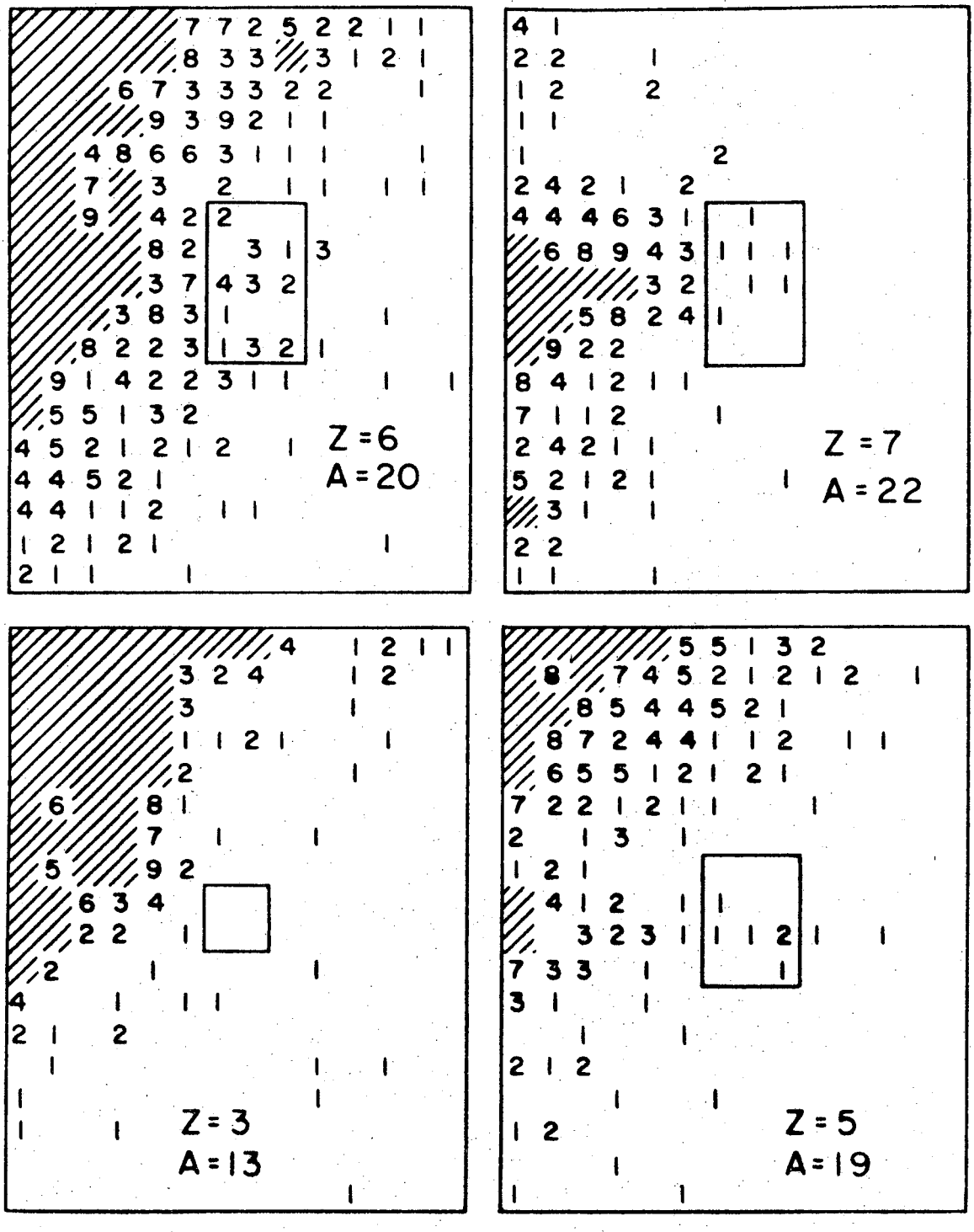

Fig. 19

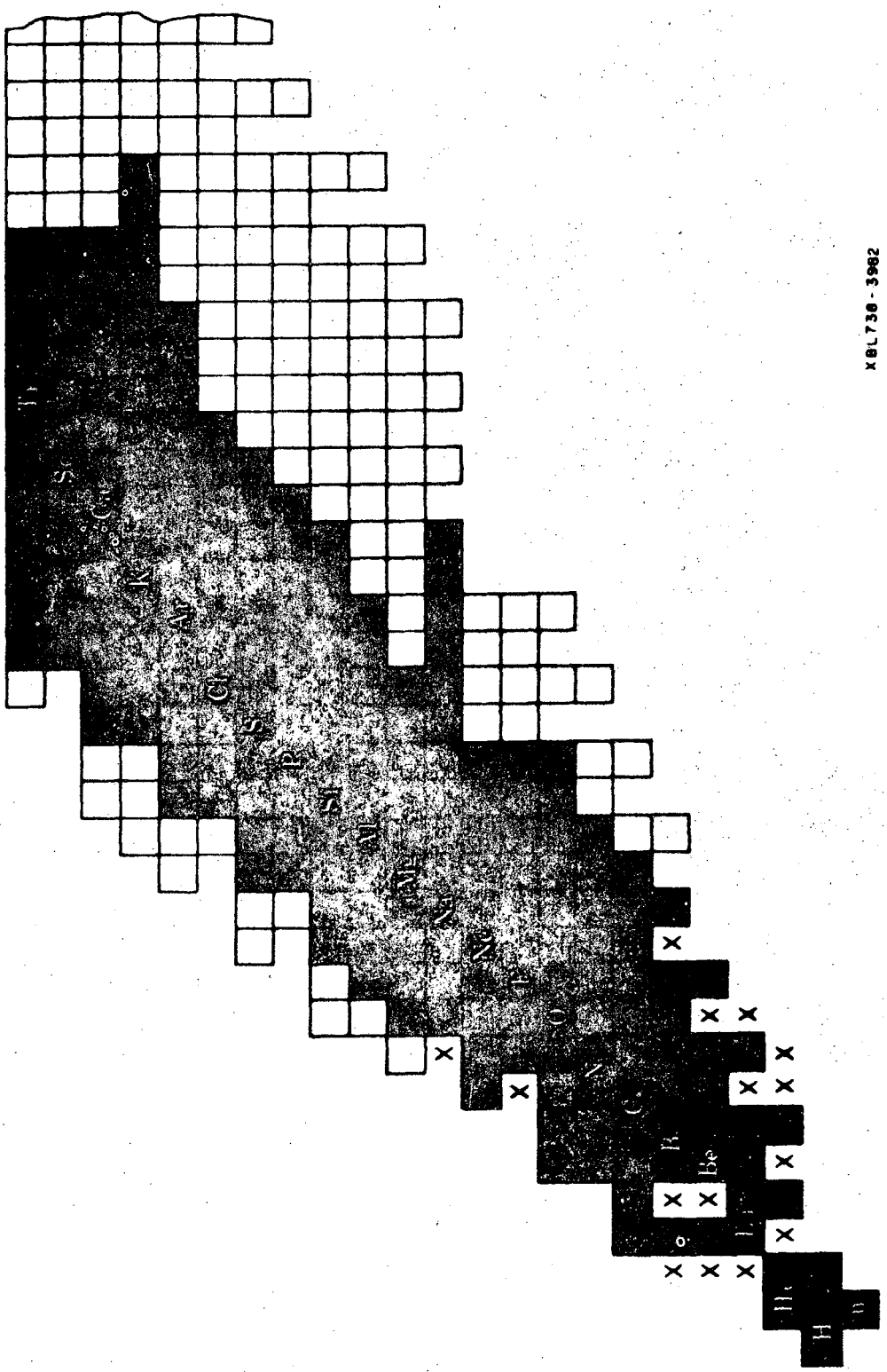

Fig. 20

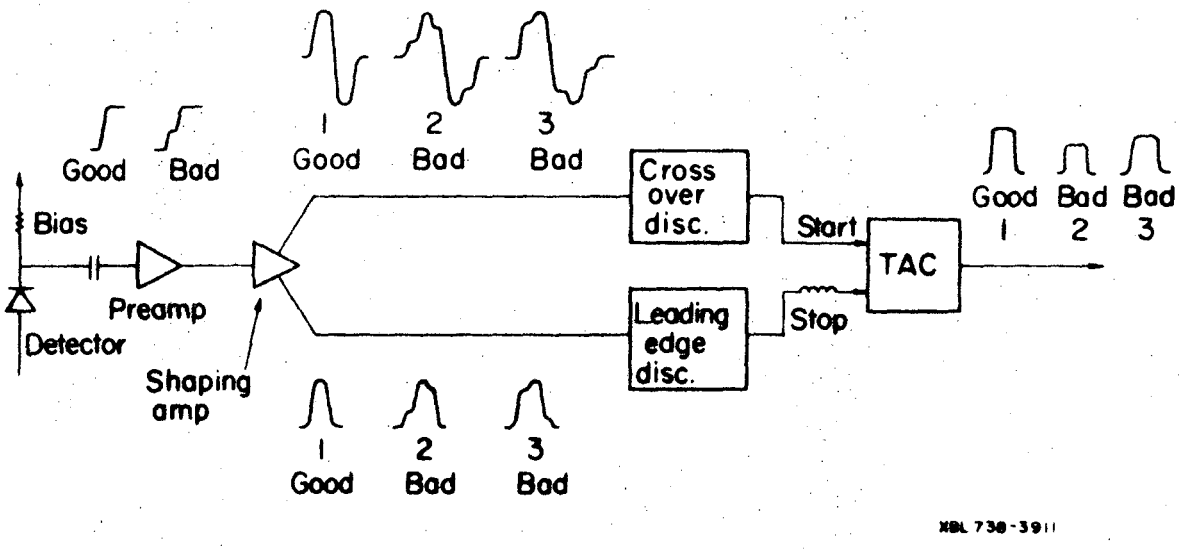
Good
Bad
1
Good
2
Bad
3
Bad
Bias
Preamp
Detector
Shaping amp
Cross over disc.
Leading edge disc.
Start
Stop
TAC
Good
1
Bad
2
Bad
3
1
Good
2
Bad
3
Bad
XBL 738-3911

Fig. 21

TECHNICAL INFORMATION DIVISION
LAWRENCE BERKELEY LABORATORY
UNIVERSITY OF CALIFORNIA
BERKELEY, CALIFORNIA 94720